

Artificial intelligence applied to the automatic analysis of absorption spectra. Objective measurement of the fine structure constant.

Matthew B. Bainbridge^{1,2*}, John K. Webb^{2†}

¹*College of Science and Engineering, University of Leicester, University Road, Leicester, LE17RH, UK.*

²*School of Physics, University of New South Wales, Sydney, NSW, 2052, Australia.*

20 January 2017

ABSTRACT

A new and automated method is presented for the analysis of high-resolution absorption spectra. Three established numerical methods are unified into one “artificial intelligence” process: a genetic algorithm (GVPFIT); non-linear least-squares with parameter constraints (VPFIT); and Bayesian Model Averaging (BMA).

The method has broad application but here we apply it specifically to the problem of measuring the fine structure constant at high redshift. For this we need objectivity and reproducibility. GVPFIT is also motivated by the importance of obtaining a large statistical sample of measurements of $\Delta\alpha/\alpha$. Interactive analyses are both time consuming and complex and automation makes obtaining a large sample feasible.

In contrast to previous methodologies, we use BMA to derive results using a large set of models and show that this procedure is more robust than a human picking a single preferred model since BMA avoids the systematic uncertainties associated with model choice.

Numerical simulations provide stringent tests of the whole process and we show using both real and simulated spectra that the unified automated fitting procedure out-performs a human interactive analysis. The method should be invaluable in the context of future instrumentation like ESPRESSO on the VLT and indeed future ELTs.

We apply the method to the $z_{abs} = 1.8389$ absorber towards the $z_{em} = 2.145$ quasar J110325-264515. The derived constraint of $\Delta\alpha/\alpha = 3.3 \pm 2.9 \times 10^{-6}$ is consistent with no variation and also consistent with the tentative spatial variation reported in Webb et al. (2011) and King et al. (2012).

Key words: quasars: absorption lines, cosmology: observations, methods: data analysis

1 INTRODUCTION

Interactive methods for analysing high-resolution quasar spectra of heavy element absorption systems are complex and require considerable expertise. Modelling even just one absorption system can be very time-consuming if the velocity structure is complex, as is the case for a typical damped Lyman- α absorption system for example (Riener-Sørensen et al. 2015).

The literature contains many examples of fits to absorption systems which are clearly inadequate, highlighting the complexity. However, if the numerical methods have been developed and applied properly, whilst the end product will not be a unique solution, it will at least be a statistically acceptable fit to the data. Parameter errors are derived from the diagonal terms of the covariance matrix, which has been shown to be reliable (King et al. 2009a). However, the derived parameter errors are strictly only valid if the model is correct.

Much of our recent work has focused on a search for space-time variation of the fine structure constant α , and

* E-mail: mbb8@le.ac.uk

† E-mail: jkw@phys.unsw.edu.au

we have presented tentative evidence for spatial variations over cosmological scales, modelled by a spatial dipole (Webb et al. 2011; King et al. 2012). Such a potentially important effect obviously needs critical checking. Any possible subjectivities associated with the analysis process must be identified and if present accounted for. The “traditional” method used to analyse the data requires significant human input and human decisions. Given the complexity of the analysis and given the methodology used, it is unlikely that the human element could introduce a systematic bias on α , especially causing a spatial dipole. Nevertheless, it is imperative to check.

One would also like to know more about the individual parameter estimates and uncertainties associated with ambiguities in the “manual” fitting of the absorption complexes used. For example, given that one cannot uniquely determine the absorbing cloud model, how robust is the α estimate to changes in the velocity structure? To address these issues, we would like the ability to explore a large set of models of the absorption line complex, mapping out the corresponding probability space for α and any other parameters of particular interest. This is the main motivation for the work described in this paper. However, the methods developed in this paper are of wider applicability.

A secondary motivation is one of practicality. A considerable amount of time is devoted to echelle spectroscopy of quasars on large optical telescopes. Whilst some analyses of such data are based on computing statistical properties of the data directly from the spectrum, e.g. power spectra to measure baryon acoustic oscillations, others require a detailed Voigt profile analysis to extract parameters associated with specific absorption lines/systems e.g. measurements of metallicity, α , T(CMB), D/H, abundance measurements. Interactive measurements with such data can be very time consuming and telescope archives (e.g. HIRES/Keck, UVES/VLT) generally contain a considerable amount of echelle spectra which either remain unpublished, or which have only been partially analysed and hence from which a great deal of valuable scientific information has yet to be extracted.

To address all these shortcomings, we have developed a new genetic algorithm that is likely to have broad application in observational cosmology, applied here specifically to the problem of modelling quasar absorption systems. It unifies a memetic “artificially intelligent” process with Bayesian Model Averaging (BMA), providing a more robust and more automated methodology, hence bringing a far greater degree of objectivity and reproducibility to the problem. The new method is used to derive a measurement of $\Delta\alpha/\alpha$ from thousands of potential models and has allowed an exploration of the stability of $\Delta\alpha/\alpha$ to model complexity. Our new method enables almost complete removal of human interaction and hence subjectivity.

The structure of this paper is as follows. In Section 2 we discuss the considerations in designing algorithms that aim to replace human decision making in the context of automated spectral fitting and explain why one in particular is highly suited. A genetic algorithm is used to apply a large set of trial models to the data and this is combined with local non-linear least-squares minimisation for each candidate model to select the fittest. In Section 3 we develop in detail this hybrid approach. Section 4 outlines a simple

simulation to test the methods. Section 5 explains how we incorporate additional free parameters and parameter constraints. Section 6 introduces our method of BMA and develops the mathematical formalism. Section 7 presents the results of applying our new methods to an absorption complex at $z_{abs} = 1.839$ towards the quasar J110325-264515, deriving a measurement of the fine structure constant in that gas cloud. A comprehensive discussion on robustness is also given. Finally in Section 10 we summarise our conclusions.

2 PRELIMINARY CONSIDERATIONS

Interactive analyses of high-resolution spectra are currently done using programs such as VPFIT (Carswell & Webb 2015). Recent papers summarising the application of VPFIT to quasar spectroscopy include King et al. (2012), Riemer-Sørensen et al. (2015) and Wilczynska et al. (2015). Small regions of the spectrum are selected by eye such that each is flanked by a sufficiently long continuum region. First guesses for the absorption line parameters are generated through trial-and-error, the efficiency depending heavily on the user expertise. Usually there is considerable blending of adjacent absorption features and the user decides on the first guesses. The human brain is good at visually filtering out random noise, picking out stationary points, inflection points, and small asymmetries, such that a reasonable guess can be made as to the velocity structure. By simultaneously visually inspecting different species aligned in velocity space, contaminating lines from different redshift systems can be identified and the set of first guesses further refined.

Nevertheless, experience shows that two people, working independently, can often produce a *different* first guess model. Their end results after least-squares minimisation can therefore also end up differently (Wilczynska et al. 2015). In the absence of any further, comprehensive, exploration of many models, there thus remains uncertainty as to the robustness of conclusions drawn from individual models.

Emulating what the human brain does so well poses interesting challenges. The eye is able to filter the random noise contribution, differentiate the observed data, and spot stationary and inflection points. The eye assesses the underlying model by simultaneously inspecting an entire spectral segment of the data, identifying the simplest underlying element, the “building block” from which the complex is constructed (i.e. a single absorption line in our case), and then reconstructing the whole spectral segment by assigning it a set of individual, varying-strength, absorption components.

Clearly a simple computer algorithm can be used to differentiate the spectrum. However this increases noise, requiring prior Weiner (or similar) filtering to help determine stationary and inflection points numerically, but then small-scale information can be lost in the smoothing process. An additional complication in converting fixed points into first guesses for parameters is the instrumental resolution, so deconvolution methods are needed. Further complications are caused by possible breaks in the data — one cannot then determine the derivatives continuously and the data has to be dealt with as fragments. Non-Gaussian noise (cosmic rays, bad CCD pixels) can also corrupt small-scale information content.

However, all the problems above can in principle be

dealt with and one can automate obtaining the first-guess parameters. Nevertheless, such a method still lacks some important aspects of the eye’s more sophisticated pattern-matching ability and therefore the end result is not as good. Nor does a deterministic method such as this provide any mechanism for exploring robustness of certain “embedded” fundamental parameters of interest, for example α , to the choice of model. To do that we need to incorporate additional search methods in order to explore a large set of candidate models. With these things in mind, we therefore initially assessed the applicability of various statistical methods to this problem, the first important decision being how best to generate candidate model databases, i.e. randomly or intelligently.

2.1 Different optimisation approaches

Parameter estimation methods can generally fall into one of the categories, deterministic, stochastic and heuristic. A deterministic algorithm will always take the same path through parameter space, producing the same result from a given starting point (Adriaan van den Bos 2007). A non-linear least-squares method such as VPFIT (Carswell & Webb 2015) is an example of a purely deterministic method. A stochastic algorithm relies on a random sampling of parameter space to reach a solution. Markov Chain Monte Carlo is an example of this type of method. This has been applied to quasar spectroscopy (King et al. 2009b) and was found useful primarily to check on the validity of covariance matrix diagonals as parameter error estimates. A heuristic algorithm conducts an “experienced-based” search of parameter space, i.e. the current search direction depends on the previous search history. Genetic algorithms involving such machine-learning or “artificial intelligence” are examples of this type of method.

Stochastic methods (Spall 2003) are insensitive to noise, unlike deterministic algorithms. Also, stochastic methods make no assumption of the objective function. The exact solution can in principle be reached although requires an infinite number of trials. Many calculations are needed and the approach is inefficient and may not be feasible for problems with a large number of free parameters.

Heuristic methods (Winker & Gilli 2004) require far fewer trial models compared to stochastic methods, hence are more efficient, and like stochastic methods, are insensitive to noise. However, because of the directed nature of the search, regions of parameter space can be left unexplored and there is no guarantee of reaching an acceptable solution.

A genetic algorithm (one type of heuristic method) offers the best features of deterministic and stochastic (Holland 1975). It reduces the number of required calculations, compared to stochastic, and because the search direction is “artificially intelligent” the optimal solution is reached more efficiently.

In some sense the genetic method reflects a manual procedure. Manually, one would initially fit the data with all the obvious features and then use some goodness-of-fit measure to make decisions about including extra parameters. The genetic method makes decisions in a similar way. Nevertheless, by itself, a genetic algorithm cannot provide the combination of efficiency and precision required for our problem.

3 A HYBRID APPROACH

In practical applications, a hybrid approach can be very effective, taking advantage of the best characteristics of the fundamentally different approaches described above e.g. Krasnogor (2010). The amalgamation of a deterministic and a heuristic technique, referred to as a “memetic algorithm” by some authors e.g. Sudholt (2009), has been widely applied and we have opted for this approach in this paper. We have chosen to use a genetic algorithm which sits “above” VPFIT, controlling a high level or global parameter space search, within which VPFIT is used for local optimisation. In this paper we refer to GVPFIT as the whole process, i.e. genetic algorithm + VPFIT.

Whilst genetic algorithms come in different varieties, the Darwinian analogies can be generalised and put in context: an iterative procedure is set up to generate a population of “individuals” (theoretical absorption cloud models in our case) and subject them to “environmental pressure” (goodness-of-fit testing) and select using “survival of the fittest” (minimum- χ^2). This results in natural selection (keeping only the best candidate model) and increasingly stronger “offspring” (a new theoretical model, slightly better than the previous). The algorithm can thus be broken down into an initialisation procedure, followed by an iterative 5-step process: Reproduction, Mutation, Local Optimisation, Selection and Evolution, illustrated in Figure 1.

The remainder of this section describes the algorithm details.

3.1 Initialisation

The setup for using GVPFIT is very similar to the VPFIT setup. The spectral data format is the same as for VPFIT (FITS or ascii). The atomic data used in the analysis in this paper is given in Tables A1, A2, A6, and A7. Model absorption profiles are produced within VPFIT. However, additional input information is needed for GVPFIT:

(i) Initialisation requires a “parent” model. The parent can be simply an “empty model” i.e. an input files containing no absorption line parameters (but it must identify which species are going to be modelled). The parent can also be more complex if there are known absorption features which “contaminate” the system being fitted. Other examples of additional parameters which may be included at this stage, before the actual absorption model has been developed, are floating zero and continuum levels;

(ii) GVPFIT search parameters may be altered from their default values (see Section 3.3.1);

(iii) Stopping criteria for the genetic search may be altered from their default values (see Section 3.6.1).

3.2 Reproduction

The “parent” is now “reproduced” M times to create the current “generation” of trial models (i.e. M copies of the parent are made). M is defined by the number of steps to be taken through absorption line parameter space (as described in the next Section).

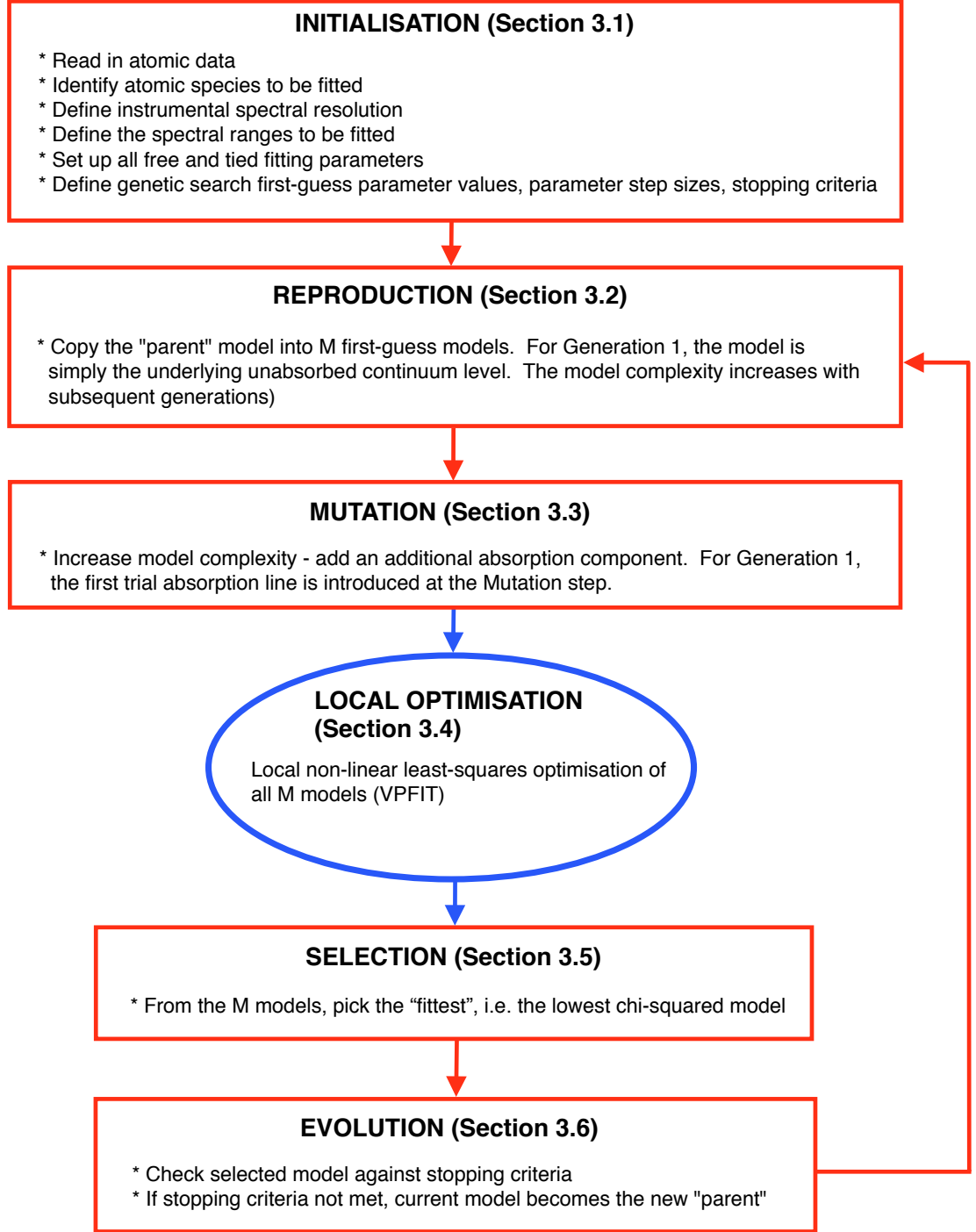


Figure 1. The whole process is the combination of a genetic algorithm and non-linear least-squares minimisation, sometimes referred to collectively as a “memetic algorithm”. Red boxes indicate the genetic part of the process that constitutes GVPFIT. The blue oval indicates standard VPFIT calls. M is the “population size” i.e. it is the total number of trial or competing models at some generation, $M = n_N \times n_b \times n_z$ i.e. the product of the number of trial values for each of the 3 variables, N, b, z .

3.3 Mutation

Each of the models in the current generation are then “mutated” by adding one additional velocity component. At the mutation step components are only added and not rejected. Component rejection only occurs during the local-optimisation stage (see Section 3.4). The parameters for the additional component are determined by the global parameter ranges and parameter step-sizes. The choice of these ranges and step-sizes determine the overall efficiency and success of the procedure (see Section 3.3.1).

Each absorption component is specified by three parameters, N, z, b . N is the column density of absorbing atoms along the line of sight, z is the absorption system redshift and b is the velocity dispersion parameter. The total number of trial models is $M = n_N \times n_b \times n_z$ (n_N, n_b, n_z are the number of trial values for column density, b-parameter and redshift).

We wish to minimise the number of calculations, but at the same time, the initial guesses must cover a range sufficiently close to the solution for a descent direction to be found by the local non-linear minimisation (Section 3.4). We carried out extensive tests, using both real data and synthetic spectra, to find suitable ranges and step sizes. The next section summarises reasonable search ranges and stopping criteria.

3.3.1 Parameter first guesses and step-sizes for the genetic algorithm

The genetic part of GVPFIT trials a range of first guess parameters which are then subject to local non-linear optimisation. Obtaining values outside the first guess range in the final fit is not precluded. The ranges in parameters discussed here are only to set the initial guesses. If the default ranges and step-sizes fail in some cases (the failure becomes obvious very quickly), these can be reset.

A reasonable lower limit for the first column density guesses is suggested by the data quality (i.e. the detection threshold). A reasonable upper limit for first guess column density can be derived from an empirical knowledge of the column density probability distribution. Absorption components for heavy elements are generally concentrated in the range $11 < \log N < 14$ but in practice we found that using $12 < \log N < 14$ for the first guess range for heavy element lines is adequate to find a non-linear minimisation search direction. For HI lines, the column density range is larger, ranging from the weaker Lyman forest lines at $\log N \approx 11$ up to the stronger damped Lyman alpha lines at $\log N \approx 21$. The genetic algorithm has also been applied to Lyman forest data but at this stage we constrained the fits to segments without strong lines, and for this we found that using $12 < \log N < 14$ for the first guess range also worked well.

Although crude, a column density step-size of $\Delta \log N = 1$ permits a reasonable computation time and does not result in the local non-linear least squares search getting stuck in local false minima.

The permitted redshift search range $z_{start} - z_{end}$ is constrained to lie within the observed wavelength range of the data. Since in general we fit multiple species simultaneously, we transform the spectral segment or segments being fitted to velocity space, $\Delta v = c\Delta\lambda/\lambda$. The starting and end points

of the velocity range are defined by the smallest and largest values amongst the input spectral segments.

Before the mutation stage, one must decide how finely to step through the redshift range, striking a compromise between computational efficiency and robustness. One would expect results to be robust within plausible step-size limits suggested by the data. For the analysis reported in Section 7, heavy elements have typical line widths of 3 or 4 km/s. The instrumental resolution (FWHM) is ~ 4 km/s. Empirically, we tried 3 step-sizes for the data in Section 7: 0.6, 1.6, and 14.5 km/s. Surprisingly, we obtained very good results even with the largest step-size (and in fact the detailed results in Tables B1 and B3 were obtained using that large step-size). The reason such a large step-size produces robust results is because local optimisation, i.e. VPFIT, is able to identify a reliable search-direction even when first-guesses are not particularly close to the local minimum.

For heavy element systems, the empirical spread in b -parameters is of the order of the typical parameter error estimates. In practice we found that taking a constant first-guesses of $b = 4$ km/s for heavy element lines worked well. For HI lines, a first guess of $b = 21$ km/s also worked well in practice.

3.4 Local optimisation (VPFIT)

Once the “local” first guesses are established, these are then subjected to local non-linear least-squares optimisation using VPFIT, (Carswell & Webb 2015).

VPFIT implements optimisation methods (Gauss-Newton or Levenberg-Marquardt) with optional parameter constraints. The method makes use of first-order derivatives of χ^2 with respect to the free parameters, and estimates of the second-order derivatives. Parameter search directions are derived by solving matrix equations involving the Hessian matrix and gradient vector. Solutions thus depend on the χ^2 derivatives being reasonably accurate. However, when the model parameters are far from the best-fit values (as can be the case in our genetic process), the derivatives will be noisy, and search directions can be poorly determined. We get around this problem by stabilising VPFIT i.e. minimising or eliminating ill-conditioning, by adding a constant value to the diagonal term of Hessian, following the procedure described in Gill et al. (1981).

Related to this is the way in which model complexity, i.e. the number of free parameters, evolves with increasing generation number. As the genetic component of GVPFIT increases complexity, trial models are sent to VPFIT for refinement. In situations where the added absorption components are such that the associated χ^2 derivatives are close to zero, and hence dominated by the finite precision of the calculation, VPFIT may fail to identify a search direction. Depending on the parameters specified in the VPFIT setup parameter file, the newly added component may then be rejected and the model complexity at that iteration remains the same. The effect of this is to cause fluctuations in the total number of free parameters, and hence a jagged appearance in the absolute χ^2 values. This can be seen in the continuous grey lines plotted Figure 7 and is a natural consequence of the overall procedure.

3.5 Selection

Following optimisation, we have a set of M trial models. In this Selection step, we select the minimum- χ^2 model which proceeds to the next step and which subsequently becomes the parent for the next generation (provided stopping criteria are not met).

3.6 Evolution

This step has 2 simple functions: (i) to check that the entire set of models so far generated comfortably spans the range of acceptable models and (ii) if not, to make the current model the new parent and then to continue iterating from the Reproduction step.

3.6.1 Stopping criteria for the genetic part of GVPFIT

As GVPFIT loops through the steps illustrated in Figure 1, the model complexity generally increases as generation number increases. To avoid this happening indefinitely, we must establish suitable stopping criteria.

The end-goal is to calculate an entire suite of potential models, such that at one extreme the models have far too few parameters to satisfactorily describe the data, and at the other extreme, have too many, i.e. the data are “over-fitted”. In other words, it does not matter when the calculations are stopped (other than economy of computing time) provided that we go well into the “over-fitting” region. After we have calculated the entire suite of models, we can then analyse the entire set to optimally extract the science data of interest.

The termination of the calculations therefore does not correspond to obtaining the “correct” or “preferred” model. The stopping criteria are required only to force the models generated to lie in a relevant range. A number of stopping criteria were explored and the following adopted.

One possibility is to simply pre-set a maximum number of generations, based on experience. If the pre-set maximum number of generations fails to reach a statistically acceptable fit, the user can simply increase the number of generations and re-start from that point. Alternatively we can establish the stopping point using a goodness-of-fit measure (for example, once χ^2_ν falls below some reasonable threshold, e.g. 0.9 or less, where ν is the number of degrees of freedom). One could define analogous conditions using other statistical measures such as the Akaike Information Criterion or the Bayesian Information Criterion (Section 6.2).

If it proves impossible to reach $\chi^2_\nu \approx 1$ irrespective of the number of pre-set generations, the input model never becomes satisfactory, one likely inference is the presence of interloping absorption lines at some other redshift. We discuss this situation separately in Section 5.

4 TESTING GVPFIT USING SIMULATED SPECTRA WITH RELATIVELY SIMPLE VELOCITY STRUCTURE

We have carried out extensive tests of GVPFIT using a broad range of simulated spectra. We avoid discussing simulations with complex velocity structure at this point in the

paper and instead describe simulations with relatively simple velocity structure that serve both as an illustration of how GVPFIT works and as a simple test.

The parameters used to generate the simulations described in this Section are given in Table 1 and in the caption to Figure 3, which shows the best fit at each generation. Figure 2 illustrates one iteration of GVPFIT, demonstrating the application of our genetic algorithm to this simple simulated spectra.

The most important conclusions of this initial simple test are: the minimum-AICc agrees extremely well with the “true” input spectrum, and this model was found within the minimum possible number of iterations, since there are 4 components in the model. Out of the 13 free parameters in the model, Table 1 shows that 11 agree to better than 1σ and the other 2 free parameters are within or close to 2σ , as expected.

In Section 9 we describe more sophisticated tests based on simulated spectra with velocity structures both simpler than and more complicated than the $z_{abs} = 1.839$ towards J110325-264515.

5 ADDITIONAL FREE PARAMETERS, PARAMETER CONSTRAINTS, INTERLOPERS

Additional free parameters may arise depending on the data attributes and on what one wants to solve for. The same additional free parameters that can be introduced in “manual” fits can be included in GVPFIT, e.g. continuum level, zero levels, velocity offsets between separate fitting regions, cloud temperature, turbulent velocity component, α . Similarly, parameter constraints (e.g. tied redshifts, tied b -parameters, summed column densities) are defined in exactly the same way as in manual fits.

5.1 b -parameter constraints

As with previous analyses, we require that the absorption line width (b -parameter, with $b = \sqrt{2}\sigma$) for a particular species in the fit is related to the corresponding components for other species. The two extremes are wholly thermal broadening ($b^2 = 2kT/M$ for a species with atomic mass M) and wholly turbulent broadening ($b^2 = b_{\text{turb}}^2$). In general, there will be contributions from the two mechanisms ($b^2 = 2kT/M + b_{\text{turb}}^2$). We discuss this further in the context of our modelling of the $z_{abs} = 1.839$ absorption system towards J110325-264515 in Section 7.7. See Carswell & Webb (2015) for further discussions of tied parameters. The fully-automated method described in this paper, i.e. GVPFIT, is therefore no less flexible than the well-established manual version, i.e. VPFIT.

5.2 Interlopers

Since each quasar sight-line generally contains many distinct absorption systems at different redshifts, blending between species at different redshifts occurs frequently. One approach to solving this complication is to carefully identify all absorption redshifts, to examine where such blends can

GENERATION 2

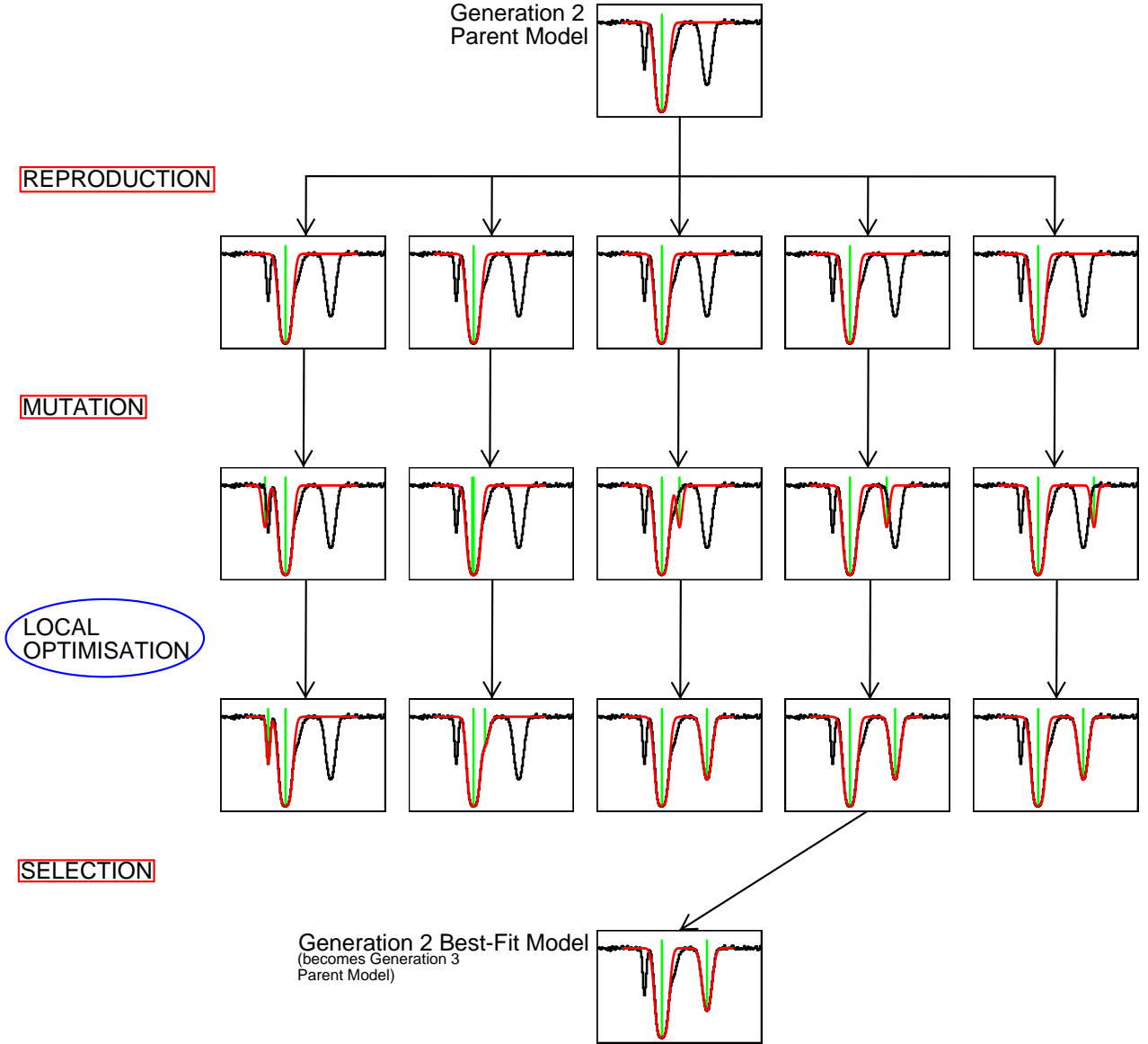


Figure 2. A simplified example to illustrate how the algorithm emulates Darwinian evolution, as portrayed in Figure 1. Shown is the second generation or iteration of GVPFIT when applied to a simple simulated spectra as part of the test described in Section 4. The data (black line) is a simple 4-component synthetic spectrum created using a spectral resolution of $\text{FWHM} = 3.2 \text{ km s}^{-1}$, a pixel size of 1.25 km s^{-1} , and the mean signal-to-noise is approximately 100. These observational parameters correspond to the real values for the 2006 data for the quasar J110325-264515 (Tables 2 and 3). Two transitions were simulated and then fitted simultaneously, FeII2600 (shown in this Figure) and 1608 (not illustrated). In this simplified example, the first-guess column density N and b -parameter remain the same each time a new trial component is introduced. 5 trial redshift positions were used. Therefore, specifically for this example, $M = 5$ (see Figure 1) and this happens to be the same as the number of trial redshifts, but this would not normally be the case. In general, $M = n_N \times n_b \times n_z$ i.e. the product of the number of trial values for each of the 3 variables, N, b, z . In the 1st row of this figure, the model (the smooth red line), is the result from Generation 1, i.e. it is the model chosen after local optimisation (VPFIT). In the 2nd row, the model has been reproduced, ready for mutation. In the 3rd row, the successful parent model has been copied from the previous step, modified by adding one extra velocity component with different redshifts. b and N are the same for the added velocity component in each case, as these are first guesses that are subsequently optimised in the next step. However, the example illustrated here has been deliberately kept simple and in general all 3 parameters are varied. The 4th row shows the result after local optimisation of each model from the 3rd row. In the example shown, the right-hand three models are visually indistinguishable. The redshift step-size is relatively coarse in this simple example, so VPFIT local optimisation produced 3 almost identical models. Finally, in the 5th row, the model shown is the best (minimum- χ^2) fit for this Generation.

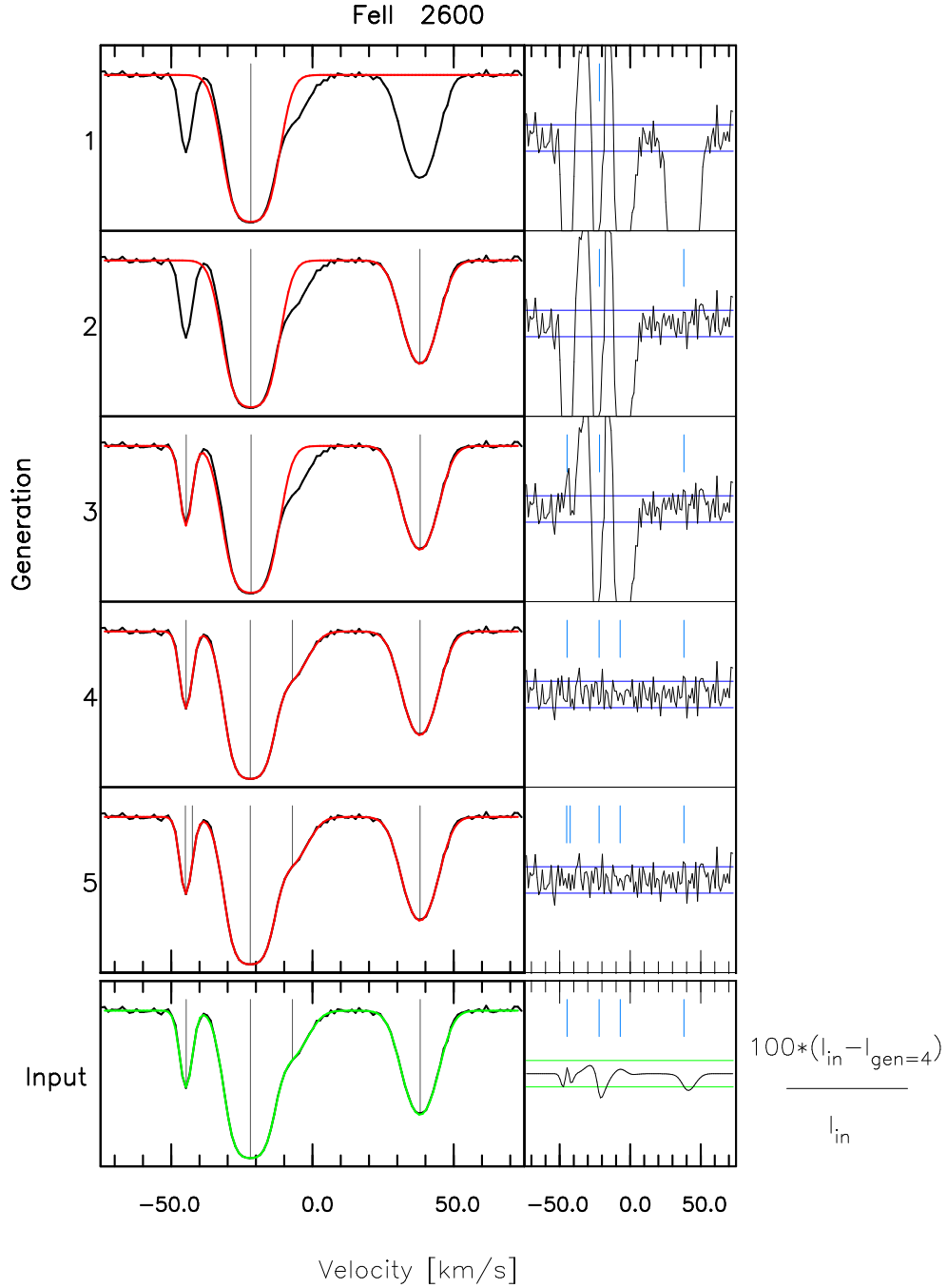


Figure 3. This illustrates the application of the genetic process to an simulated spectrum with known parameters. We simulated 2 FeII transitions (2600 and 1608Å) with 4 velocity components. Only FeII 2600 is illustrated here. The absorption line parameters used to create the model are given in Table 1. The signal-to-noise used is approximately 100 and the spectral resolution is $\sigma = 1.6$ km/s (as per the 2006 data). In the upper 5 left-hand panels, the spectral data are shown in black and the best-fit model at each generation in red, I_{gen} . Grey vertical ticks show the position of absorption components at each generation. The upper 5 right-hand panels illustrate the normalised residuals and the horizontal blue lines show 1σ bounds. Each of generations 1 through 5 in this Figure corresponds to 5 iterations of the “EVOLUTION” step in Figure 1. The genetic process found a satisfactory solution in 4 generations, plotted here on a velocity scale. In practice, we ran GVPFIT for 10 generations. Generations 6-10 appear visually almost identical so we only plot the first 5. The lowest (6th) left-hand panel illustrates the “true” spectrum, I_{in} and the corresponding right-hand panel plots the blown-up fractional difference $(I_{in} - I_{gen=4})/I_{in} \times 100$. In the same panel, the horizontal green lines show a fractional flux difference of 1%. A comparison between the input and output parameters is given in Table 1. The minimum-AICc model was found within the minimum possible number of iterations, since there are 4 components in the model.

Table 1. Here we show the results of applying GVPFIT to the simple simulated spectrum shown in Figure 3 and discussed in Section 4. The absorption line parameters for the input model and the best-fit (minimum AICc) parameters derived using GVPFIT are tabulated. The statistical uncertainties, as determined by VPFIT, are also given. Input model: Four-component absorption system comprising only two transitions: FeII 1608 and FeII 2600. In the input model, $\Delta\alpha/\alpha$ was set to 2.6×10^{-6} . The total number of free parameters in the model = 13. The number of data points = 239 and the number of degrees of freedom is therefore = 226. The best-fit α parameters are: $\Delta\alpha/\alpha = (0.7 \pm 1.8) \times 10^{-6}$, $\chi^2 = 211.8$. The first column gives the velocity component number. Columns 2 and 3: redshift parameters; Columns 4 and 5: Doppler parameters; Columns 6 and 7: FeII column density. Out of the 13 free parameters in the model, 11 agree to better than 1σ , and the other 2 free parameters are within or close to 2σ , as expected from Gaussian statistics.

#	z_{input}	z_{fitted}	b_{input} [kms ⁻¹]	b_{fitted} [kms ⁻¹]	N_{input} log ₁₀ [cm ⁻²]	N_{fitted} log ₁₀ [cm ⁻²]
1	1.8383248	1.8383245 ± 0.0000005	1.84	1.77 ± 0.07	12.4166	12.4178 ± 0.0064
2	1.8385399	1.8385395 ± 0.0000004	6.62	6.64 ± 0.03	13.5948	13.5937 ± 0.0014
3	1.8386810	1.8386810 ± 0.0000018	6.94	6.85 ± 0.26	12.4404	12.4390 ± 0.0149
4	1.8391085	1.8391085 ± 0.0000005	7.03	7.02 ± 0.04	12.9853	12.9811 ± 0.0020

occur, and then to simultaneously fit all relevant parameters. Nevertheless, it may not always be possible to identify all absorption systems present and an unidentified interloping absorption line or lines can blend with transitions of interest. This may be revealed as a poor goodness-of-fit for the blended spectral region. Manually, in this circumstance, one would then guess at the positions, strengths and number of interloping velocity components, and allow VPFIT to iterate to a best-fit solution (Carswell & Webb (2015)).

In some cases, a statistically acceptable fit may be obtained, yet a weak interloper may nevertheless be present. A conservative approach when using GVPFIT is therefore to *assume* interlopers are present (i.e. without needing to identify them beforehand) and allow GVPFIT to search parameter space for interlopers.

The application of GVPFIT is then as follows. First we carry out a complete GVPFIT assuming no interlopers are present. Then we select a preferred model using AICc. We note that selecting a preferred model does not follow the spirit of using BMA (Section 6) but it is nevertheless a useful thing to do in this context. That preferred model is then used as a parent (in the sense of Section 3) and GVPFIT is applied again but is only allowed to add interlopers as unidentified species (i.e. it is prevented from adding further metals, MgII for example).

The result of this process may or may not end up identifying any interlopers (for the absorption system analysed in this paper, it did – See Section 7.8).

If an interloper is found and is blended with some transition of interest, it could potentially bias the measurement of $\Delta\alpha/\alpha$. It is then necessary to quantify this potential bias. There are several ways in which this could be done. In this paper we adopt the following very simple approach and avoid a general discussion outlining other possible methods.

Having identified the interloper or interlopers and having found best-fit parameters for them using the preferred model, we could “insert” the interlopers into the underlying continuum and re-run the entire GVPFIT process with the interlopers as fixed parameters. In practice, for the absorption system analysed in this paper, that was unnecessary, as explained in Section 7.8.

5.3 Weak lines and ill-conditioning

As described in Section 3.6.1, as GVPFIT evolves the fit into the “over-fitting” regions the model may include one

or more very weak absorption components that have large parameter error estimates. When that happens, logarithmic error estimates on column densities can be large. Finite-difference derivatives of χ^2 with respect to those parameters can then be close to zero and thus dominated by machine noise (i.e. rounding errors). The effect of that is to produce ill-conditioning in the Hessian matrix, potentially making the non-linear least-squares optimisation unreliable (Gill et al. 1981). This in turn can impact adversely on the ability to correctly determine the parameter estimates (and uncertainties) for the “good” velocity components. However, it is easy to check for this effect. When such large parameter error estimates are spotted, one can re-run the model but with those particular parameters fixed. This then removes any possibility of throwing noise into the Hessian and gradient vector. If the parameter estimates and associated error estimates for the parameters of interest are unchanged by this process, ill-conditioning is unimportant.

6 POST-FITTING ANALYSIS

6.1 Bayesian Model Averaging

The methodology outlined above produces a large set of possible models, many of which are statistically acceptable representations of the data. The question then naturally arises as to how to select *one* parameter, or range of parameters, deemed to be “correct”, or at least the best, solution. Should we chose one preferred model or is it better to select a set of models? The former is the current VPFIT methodology. The latter represents a fundamentally different approach.

It has been noted that averaging over all the candidate models provides better predictive ability than using any single model (Leamer (1978); Draper (1995); Hodges (1987)). The improvement provided by model averaging, as opposed to selecting one preferred model, has been quantified using a logarithmic scoring rule (Raftery et al. 1997) — see Hoeting et al. (1999) for a review describing empirical support for this method. In this Section we describe how to average over a large set of models to derive robust parameter estimates.

Let \mathbf{x} be the set of parameters describing the data. In our case we are particularly interested in $\Delta\alpha/\alpha$, one of the parameters contained within the vector set \mathbf{x} . Let \mathbf{D} be the spectrum i.e. $\mathbf{D} = \{d_i\}$ (d_i being the intensity at the i^{th} pixel in the spectrum). Let $\mathcal{M}_j = \{I(\mathbf{x})_i\}_j$, where $I(\mathbf{x})_i$ is

the model intensity at the i^{th} pixel, i.e. \mathcal{M}_j is the j^{th} model of the data.

Given the spectrum \mathbf{D} and some particular model \mathcal{M}_j , the posterior weighted average of the parameter set \mathbf{x} is (Raftery et al. 1997; Hoeting et al. 1999)

$$p(\mathbf{x}|\mathbf{D}) = \sum_{i=1}^S p(\mathbf{x}|\mathbf{D}, \mathcal{M}_j) p(\mathcal{M}_j|\mathbf{D}) \quad (1)$$

where the summation is taken over all S models (i.e. we sum over all models within all generations), $p(\mathbf{x}|\mathbf{D}, \mathcal{M}_j)$ is the probability of obtaining the parameters \mathbf{x} given \mathbf{D} and \mathcal{M}_j and $p(\mathcal{M}_j|\mathbf{D})$ is the probability that \mathcal{M}_j is the correct model given the data \mathbf{D} (assuming that the correct model is in fact in the list of models),

$$p(\mathcal{M}_j|\mathbf{D}) = \frac{p(\mathbf{D}|\mathcal{M}_j)p(\mathcal{M}_j)}{\sum_{l=1}^S p(\mathbf{D}|\mathcal{M}_l)p(\mathcal{M}_l)} \quad (2)$$

The expected value and variance of \mathbf{x} is then (Hoeting et al. 1999),

$$E[\mathbf{x}|\mathbf{D}] = \sum_{i=1}^S E[\mathbf{x}|\mathbf{D}, \mathcal{M}_j] p(\mathcal{M}_j|\mathbf{D}) \quad (3)$$

and

$$\begin{aligned} \text{Var}[\mathbf{x}|\mathbf{D}] = & \sum_{j=1}^S (\text{Var}[\mathbf{x}|\mathbf{D}, \mathcal{M}_j] \\ & + E[\mathbf{x}|\mathbf{D}, \mathcal{M}_j]^2) p(\mathcal{M}_j|\mathbf{D}) - E[\mathbf{x}|\mathbf{D}]^2 \end{aligned} \quad (4)$$

6.2 Three statistics

The above formulation requires us to compute the probability of obtaining the j^{th} model, given the data \mathbf{D} , i.e. we need to compute $p(\mathbf{D}|\mathcal{M}_j)$. We use three different statistics in our analysis: chi-squared, χ^2 , Akaike Information Criterion corrected for finite sample sizes, $AICc$, and the Bayesian Information Criterion, BIC . Whilst all three statistics provide a measure of the goodness of fit to the data, χ^2 decreases with the addition of free parameters, requiring the user to decide when a satisfactory representation of the data has been achieved. $AICc$ and BIC both compensate for the addition of free parameters, but BIC has a stronger penalty and is thus more prone to under-fitting (i.e. too few parameters) compared to $AICc$.

(i) *Chi-squared, χ^2*

We use the absolute (not the normalised) quantity,

$$\chi_j^2 = \sum_i^n (\{I(\mathbf{x})_i\}_j - d_i)^2 / \sigma_i^2 = -2 \ln \mathcal{L}(\chi_j^2) \quad (5)$$

where $I(\mathbf{x})_i$ is the intensity at the i^{th} pixel in the data, \mathbf{x} is the vector set of model parameters, n is the number of data points, d_i is the model intensity at the i^{th} pixel, σ_i is its estimated uncertainty, and $\mathcal{L}(\chi_j^2)$ is the associated likelihood.

(ii) *Akaike Information Criterion corrected for small sample size, $AICc$*

The standard AIC (Akaike 1973) is

$$AIC_j = \chi_j^2 + 2k \quad (6)$$

where k is the number of free parameters. The corrected AIC allows for finite sample size (Hurvich & Tsai 1989) and is

$$AICc_j = AIC_j + \frac{2k(k+1)}{(n-k-1)} = -2 \ln \mathcal{L}(AICc_j) \quad (7)$$

where k is the number of free parameters, n is the number of data points, and $\mathcal{L}(AICc_j)$ is the associated likelihood.

(iii) *Bayesian Information Criterion, BIC*

The Bayesian Information Criterion (Bozdogan 1987) is,

$$BIC_j = \chi_j^2 + k \ln(n) = -2 \ln \mathcal{L}(BIC_j) \quad (8)$$

where k is the number of free parameters, n is the number of data points and $\mathcal{L}(BIC_j)$ is the associated likelihood.

6.3 Implementation

We assume that each model is equally likely, i.e. before considering the data we adopt a uniform prior, such that $p(\mathcal{M}_j)$ and $p(\mathcal{M}_l)$ cancel out in equation (2),

$$p(\mathcal{M}_j|\mathbf{D}) = \frac{p(\mathbf{D}|\mathcal{M}_j)}{\sum_{l=1}^S p(\mathbf{D}|\mathcal{M}_l)} \quad (9)$$

so $p(\mathcal{M}_j|\mathbf{D})$ becomes a simple model weighting function and the expectation value and variance become

$$E[\mathbf{x}|\mathbf{D}] = \sum_{i=1}^S E[\mathbf{x}|\mathbf{D}, \mathcal{M}_j] \omega_j \quad (10)$$

and

$$\begin{aligned} \text{Var}[\mathbf{x}|\mathbf{D}] = & \sum_{j=1}^S \left(\text{Var}[\mathbf{x}|\mathbf{D}, \mathcal{M}_j] \right. \\ & \left. + E[\mathbf{x}|\mathbf{D}, \mathcal{M}_j]^2 \right) \omega_j - E[\mathbf{x}|\mathbf{D}]^2 \end{aligned} \quad (11)$$

The weighting function ω_j depends on the statistical criteria used. Relating the statistical criteria to the model likelihoods, taking χ^2 as an example,

$$p(\mathbf{D}|\mathcal{M}_i) = \mathcal{L}(\chi_j^2) = e^{-\chi_j^2/2} \quad (12)$$

The weighting function (relative likelihood) for the χ^2 statistic then becomes

$$\omega(\chi_j^2) = \frac{\mathcal{L}(\chi_j^2)}{\sum_{l=1}^S \mathcal{L}(\chi_l^2)} = \frac{e^{-\chi_j^2/2}}{\sum_{l=1}^S e^{-\chi_l^2/2}} \quad (13)$$

with analogous equations for the $AICc$ and BIC statistics.

7 MEASUREMENT OF THE FINE STRUCTURE CONSTANT AT $z_{abs} = 1.839$ TOWARDS J110325-264515

7.1 Background

The $z_{abs} = 1.839$ absorption system towards J110325-264515 is an ideal target to illustrate the method presented

in Section 3. Several analyses of $\Delta\alpha/\alpha$ in this absorption system have been published (See [Levshakov et al. \(2005, 2007\)](#); [Molaro et al. \(2008\)](#); [Levshakov et al. \(2009\)](#); [King et al. \(2012\)](#)) permitting a direct comparison between the previous methodologies and the genetic algorithm presented in this work (See Section 6). The spectral data are high signal-to-noise and high spectral resolution (3) and the absorption system is relatively complex and thus presents a good challenge to our new method.

In addition, the combination of MgII and FeII absorption, including the particularly important FeII1608 transition (because of its opposite-sign sensitivity to α compared to other FeII transitions — see Table A2), makes this system unusually sensitive to $\Delta\alpha/\alpha$, giving added motivation to a detailed analysis of this absorption system.

7.2 The observational data

The quasar J110325-264515 has an emission redshift of 2.145 and an apparent magnitude (in B, V and R) of approximately 16 ([Osmer & Smith 1977](#)). Early high-resolution spectroscopic studies of this quasar include [Carswell et al. \(1982, 1984, 1991\)](#). The observational data used in the analysis presented in this paper were obtained using the Ultra-Violet Echelle Spectrograph on the Very Large Telescope (UVES/VLT) ([Dekker et al. 2000](#)).

There have been three separate observations runs towards J110325-264515, 2000a, 2000b, and 2006. The instrumental settings were different for each. In Table 2 we summarise the details by grouping exposures according to instrumental setting. Exposure groupings numbered 1–4 were obtained using a slit-width of 0.80 and 0.90 arcsecond and 1x2 CCD binning. Groupings numbered 5–8 had a 1.00 arcsecond slit and 2x2 binning. Groupings 9 and 10 had a 0.50 arcsecond slit and 1x1 binning. Therefore we do not combine these data into a single spectrum and instead maintain 3 independent spectra which are then modelled simultaneously in our analysis.

There is a single data grouping with a slit-width of 0.90 (line 1 from Table 2). We have merged this data grouping with the 0.80 slit width exposures from the same year (line 2–4 from Table 2) instead of separating it into a fourth co-added spectra.

Figure 4 shows these three co-added spectra and illustrates where the transitions used fall (green vertical lines) and where other transitions were discarded because of suspected data problems (red vertical lines).

7.3 Data reduction

The spectra were extracted from 2d echelle format to 1d orders using the ESO pipeline ([Larsen et al. 2015](#)). Wavelength calibration made use of the ThAr line list from [Murphy et al. \(2007\)](#). Order combination, co-addition of multiple exposures to make the final 1d co-added spectra, and continuum fitting, were done using UVES_POPLER ([Murphy 2010](#)).

The MIDAS pipeline underestimates the $1\text{-}\sigma$ spectral error array near zero flux, impacting mostly at the base of saturated absorption lines. The effect is easily confirmed by fitting a straight (zero flux) line within the saturated

part of an absorption line and calculating the normalised chi-squared, typically found to be around 2. We correct the spectral error arrays using the procedure described in Section 2.1 of [King et al. \(2012\)](#).

7.4 Transitions used to measure α

We identified 32 transitions comprising the redshift 1.839 absorption system: AlII, AlIII, CII, CIV, CII, FeII, FeIII, HI, MgI, MgII, OI, SiII, SiIII and SiIV. In this paper we focus on the FeII and MgII transitions because of their similar ionisation potentials.

Between the three observation runs, there are 18 usable spectral regions containing FeII and MgII transitions at redshift 1.839 (see Table 3).

The FeII 2586 transitions are present in our data in only the 2000a and 2006 data. Unfortunately both of these spectral regions show apparent observational glitches (perhaps due to cosmic rays or some other corruption of the raw data) in the strongest velocity component and we have not used either. The same is true for the FeII 2382 transition in 2000a. The FeII 1096 transition is barely detectable and its sensitivity to a variation on α (q-coefficient) has not yet been calculated. The five data regions that were omitted are indicated in the Comment column in Table 3.

The instrument profile was taken from the Ultra-Violet Echelle Spectrograph user manual ([Dekker et al. 2000](#)).

7.5 Atomic data

The laboratory wavelengths of the FeII and MgII transitions have recently been re-measured. We use the most recent and most precise MgII laboratory wavelengths ([Batteiger et al. 2009](#)), and the most recent and most precise FeII wavelengths ([Nave 2012](#)). In generating model absorption profiles, we use the $^{25}\text{MgII}$ 3s to 3p hyperfine structures (see Appendix A).

7.6 Choice of fitting regions

It is important to ensure that absorption regions are flanked by adequate continuum regions when fitting ([Wilczynska et al. 2015](#)). Doing this makes it less likely to miss weak lines on the system edges, more likely to anchor the broader velocity components, and will result in a more robust estimate of a floating continuum level, if included in the fitting parameters.

The final wavelength ranges for the fitting regions used in this paper are tabulated in Table B2 and illustrated in Figure 8. The weaker FeII lines include seemingly over-generous continuum regions (i.e. in the approximate regions $-180 < v < -80$ km/s). These regions provide extra column density constraints (albeit weak) and the number of free parameters (i.e. number of velocity components) is well-defined (using the AICc) by the stronger FeII transitions.

7.7 Line Broadening

We do not know *a priori* whether this absorption system is best represented by a thermal model, a turbulent model, or a hybrid of each (Section 5). In this analysis we are only

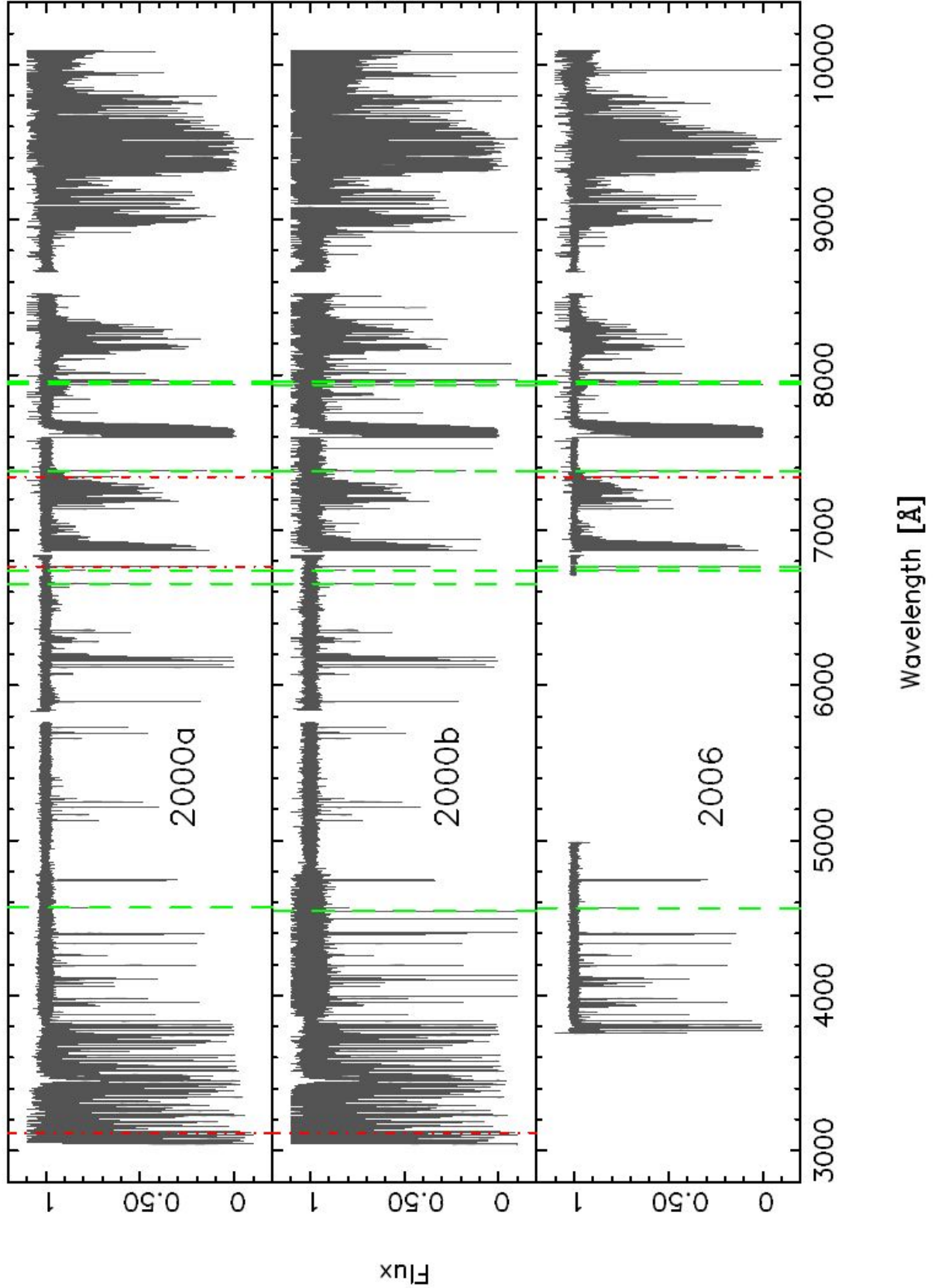


Figure 4. Illustration of the three combined spectra. Table 2 gives the observing dates and parameters for the quasar observations of J110325-264515 using UVES on the VLT. There are 10 groupings of exposures, co-added to make three spectra. Vertical green dashed lines illustrate the positions of the transitions used in our analysis. Vertical red dot-dashed lines illustrate 5 transitions that are present in the spectra but which have not been included in the analysis, either because of suspected data problems or because no q -coefficient is available (see Table 3).

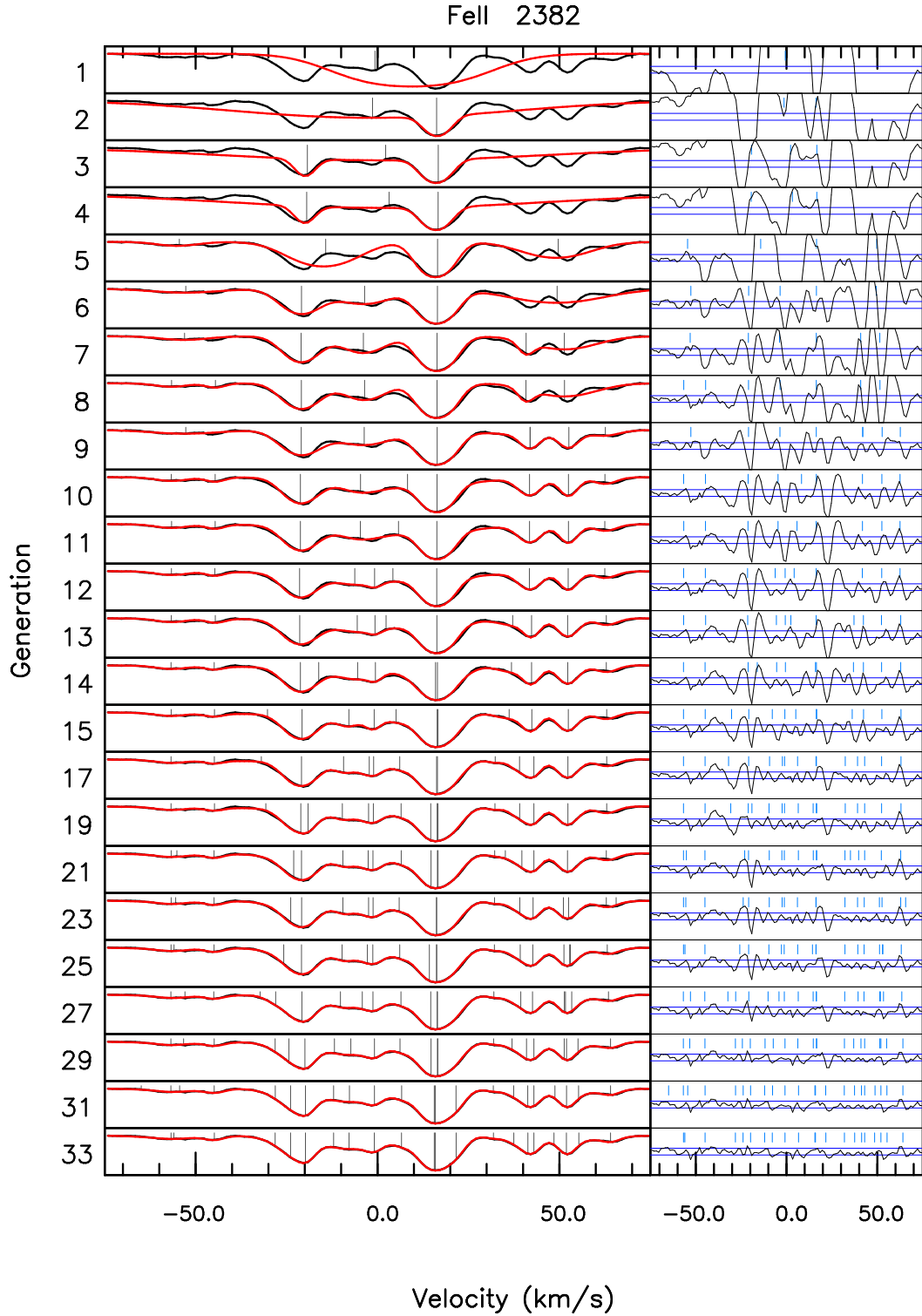
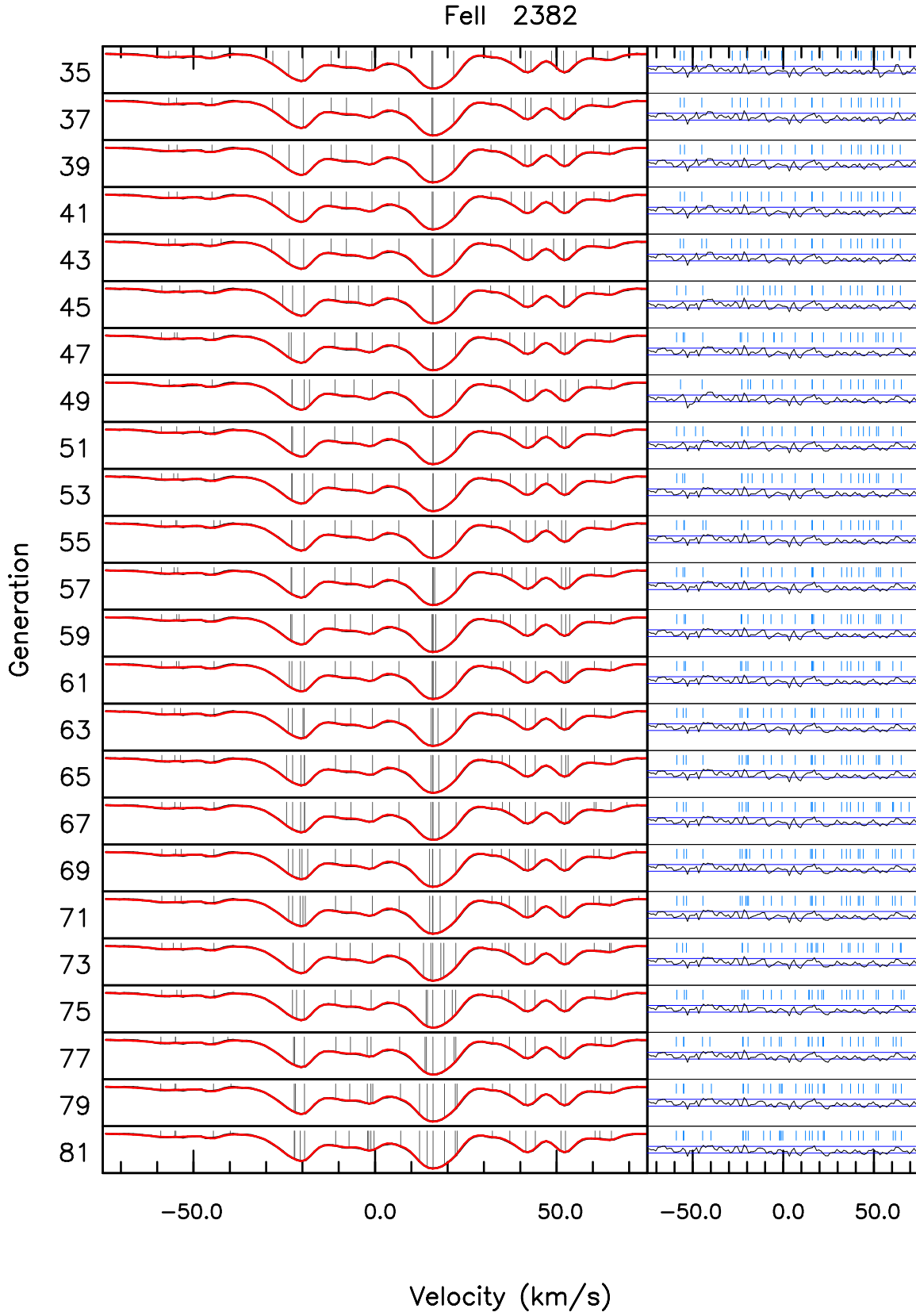
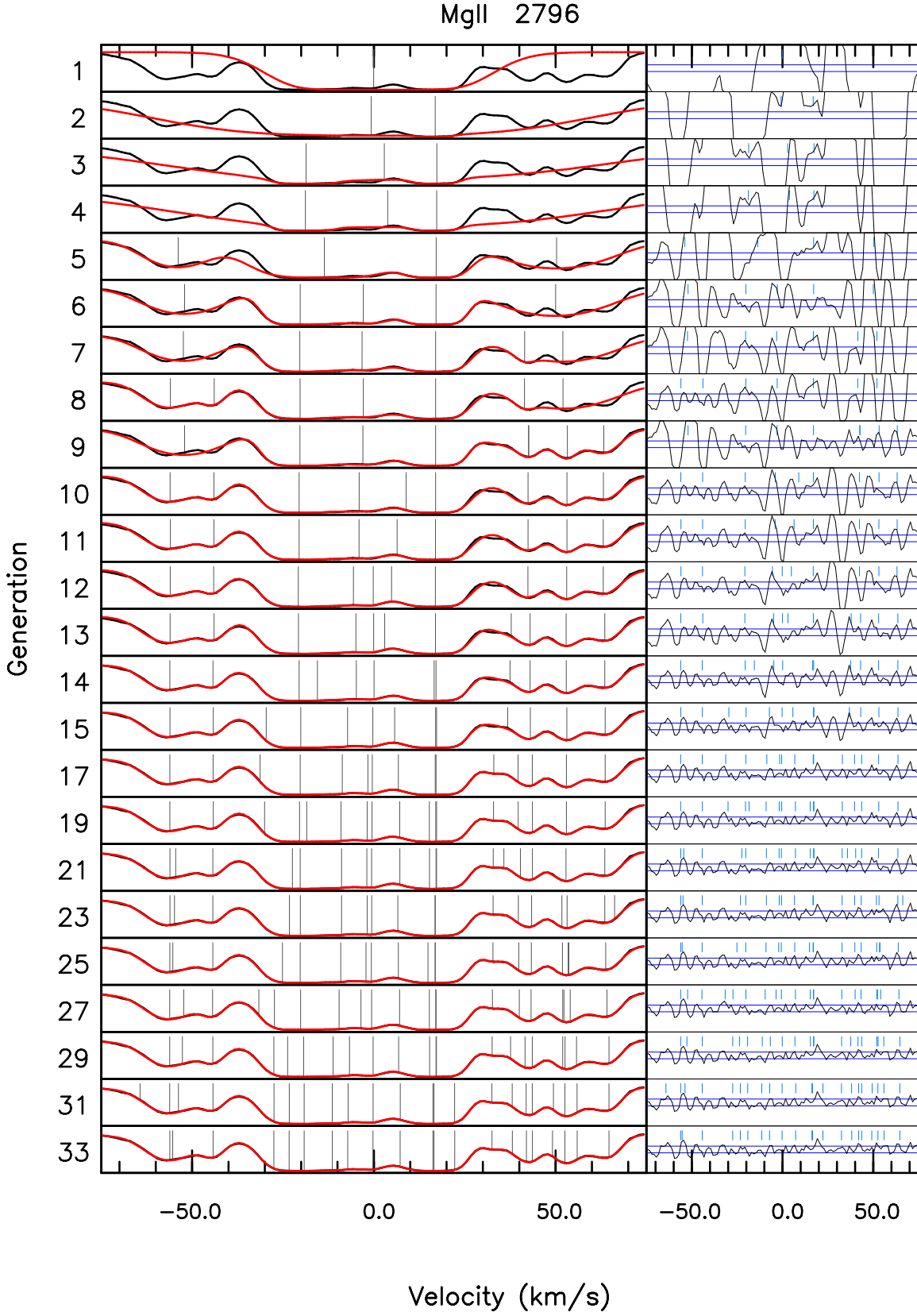


Figure 5. Evolution of minimum- χ^2 models. This figure shows how the complexity of the model absorption profile evolves with each successive generation. Shown are the best-fit model from generations 1–15 and then every odd numbered generation from 15–81. The minimum- χ^2 model (selected from the whole set of turbulent and thermal models) is displayed for each generation until generation 81. Each model was fitted simultaneously to all 6 FeII and 2 MgII transitions listed in Table 3. This figure contains a series of four plots. In the first two plots we illustrate how the fit evolved over generations 1 to 81 for the strongest iron transition, FeII 2382. In the last two plots we illustrate the same thing for MgII 2796. In the left column, the spectral data are shown in black and the model as the smooth red line. In the right column, the normalised residuals are shown, plotted over the same velocity range (but on a smaller scale). Blue horizontal lines illustrate the $\pm 1\sigma$ expectation values. Vertical ticks (grey in the left column, light blue in the right column) show the positions of absorption components at each generation.

Figure 5 – *continued*. Evolution of minimum- χ^2 models.

Figure 5 – *continued*. Evolution of minimum- χ^2 models.

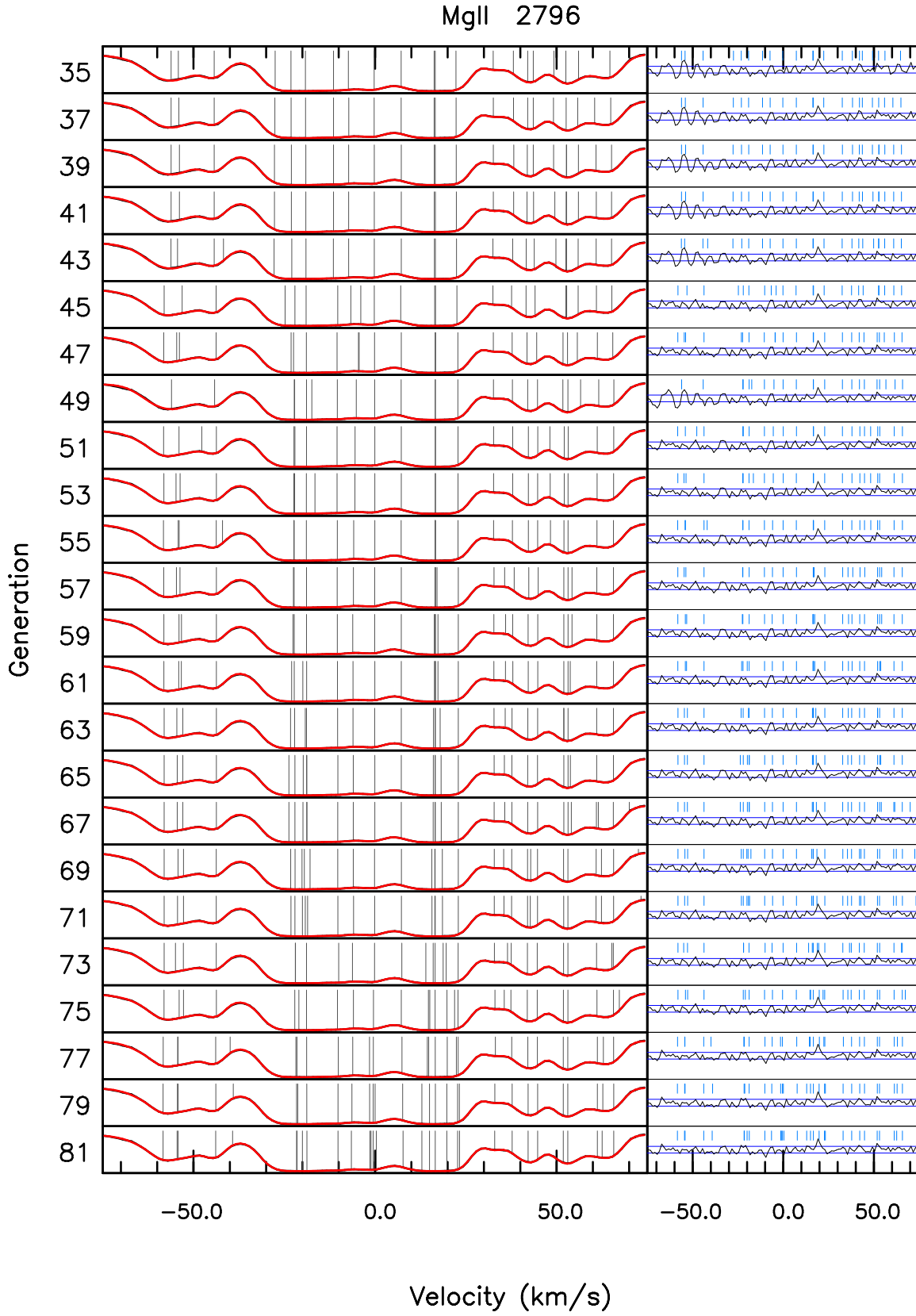
Figure 5 – *continued*. Evolution of minimum- χ^2 models.

Table 2. Observational details for the quasar J110325-264515. Column 1: data grouping. Column 2 and 3: observation date range. Column 4: total exposure time. Column 5: number of exposures. Column 6: slit width. Column 7: UVES spectrograph grating setting (central λ in nm). Column 8: on-chip binning (e.g. 1x2 = no binning in the spectral direction, 2 pixels binning in the spatial direction). Column 9: astronomical seeing. Column 10: label for co-added spectrum used in Figure 4 and Table 3. The data groupings which contribute to each of the three co-added spectra are separated by horizontal lines and these co-added spectra are illustrated in Figure 4.

#	Date from yyyy-mm-dd	Date to yyyy-mm-dd	Exp. Time [s]	# of Exp.	Slit Width [arcsec]	Setting	Bin.	Seeing [arcsec]	Spectrum
1	2000-02-11	2000-02-12	16200.008	4	0.90	346	1x2	0.62	2000a
2	2000-02-11	2000-02-16	18000.015	9	0.80	437	1x2	0.86	2000a
3	2000-02-11	2000-02-12	16199.997	4	0.80	580	1x2	0.61	2000a
4	2000-02-11	2000-02-16	17999.998	9	0.80	860	1x2	0.87	2000a
5	2000-02-10	2000-02-12	7200.004	2	1.00	346	2x2	0.73	2000b
6	2000-02-10	2000-02-10	3600.002	1	1.00	437	2x2	0.99	2000b
7	2000-02-10	2000-02-12	7200.000	2	1.00	580	2x2	0.72	2000b
8	2000-02-10	2000-02-10	3600.000	1	1.00	860	2x2	0.98	2000b
9	2006-02-21	2006-02-23	55261.009	5	0.50	437	1x1	0.87	2006
10	2006-02-21	2006-02-23	54271.992	5	0.50	860	1x1	0.88	2006

Table 3. FeII and MgII transitions in the $z = 1.839$ absorption system towards J110325-264515. Column 2: spectrum label. Column 3: species label. Column 4: transition label. Column 5: pixel size. Column 6: instrumental resolution. Column 7: observed central wavelength of absorption system. Column 8: average signal-to-noise ratio per pixel. Column 9: comments for data regions.

#	Spectrum	Spec.	Tran.	Disp. [kms ⁻¹]	Res. σ [kms ⁻¹]	λ_{center} [Å]	SNR	Comment
1	2000a	Fe II	1096	2.50	2.3	3113.7	13	not used – no q
2	2000a	Fe II	1608	2.50	2.3	4565.9	74	
3	2000a	Fe II	2344	2.50	2.3	6654.6	101	
4	2000a	Fe II	2374	2.50	2.3	6740.4	136	
5	2000a	Fe II	2382	2.50	2.3	6764.0	128	not used – suspected data problem
6	2000a	Fe II	2586	2.50	2.3	7342.8	95	not used – suspected data problem
7	2000a	Fe II	2600	2.50	2.3	7381.1	91	
8	2000a	Mg II	2796	2.50	2.3	7937.2	71	
9	2000a	Mg II	2803	2.50	2.3	7957.6	60	
10	2000b	Fe II	1096	2.50	2.7	3113.7	12	not used – no q
11	2000b	Fe II	1608	2.50	2.7	4565.9	36	
12	2000b	Fe II	2344	2.50	2.7	6654.6	68	
13	2000b	Fe II	2374	2.50	2.7	6740.4	87	
14	2000b	Fe II	2600	2.50	2.7	7381.1	46	
15	2000b	Mg II	2796	2.50	2.7	7936.8	37	
16	2000b	Mg II	2803	2.50	2.7	7957.6	29	
17	2006	Fe II	1608	1.25	1.6	4564.1	103	
18	2006	Fe II	2374	1.25	1.6	6737.7	153	
19	2006	Fe II	2382	1.25	1.6	6761.3	117	
20	2006	Fe II	2586	1.25	1.6	7339.8	145	not used – suspected data problem
21	2006	Fe II	2600	1.25	1.6	7378.2	110	
22	2006	Mg II	2796	1.25	1.6	7936.9	128	
23	2006	Mg II	2803	1.25	1.6	7957.2	99	

considering 2 species, MgII and FeII. In such a situation the degeneracy between b-parameters and temperature is too severe to solve independently for temperature (and hence solve for a hybrid model). In previous analyses, the approach has been to first develop and solve for a turbulent model and then to use that turbulent model as the starting point for developing a thermal model (because of the human time required). However in the analysis presented here, both thermal and turbulent models have been constructed independently. To our knowledge, this is the first time that this has been done.

7.8 Obtaining a consistent velocity structure for all atomic species at $z_{\text{abs}} = 1.839$ towards J110325-264515

The model here includes only two species, MgII and FeII. In order to force a consistent velocity structure for both species, we followed the procedure described in Section 5.2. One interloper was found, illustrated as a green dashed vertical line at approximately +125 km/s in Figure 8. In this particular case, it is obvious that the interloper is not going to impact on the $\Delta\alpha/\alpha$ estimate so we did not bother to follow the last part of the (more general) procedure outlined in Section 5.2, i.e. we did not enter the interloper parameters as fixed and re-run GVPFIT.

Interestingly, for this particular absorption system, there did not appear to be any velocity components with MgII above the detection threshold and FeII below, otherwise the interloper procedure (Section 5.2) would have identified them. The weak interloper that was found is detected only in MgII 2803 and not in MgII2796 so cannot be MgII. Looking at the detail in the MgII panels of Figure 8, there is an apparent difference between the interloper strength and position for the 2000a and 2006 spectra. We presume there are data problems in the 2000a spectrum at that point but made no attempt to mask data as the feature is well offset from the metal features relevant to $\Delta\alpha/\alpha$.

7.9 Results

In the analysis described here we use VPFIT Version 10, coupled with the new genetic algorithm GVPFIT.

Figure 5 shows how the model evolves at each generation. Each sub-plot in these figures illustrates the “most successful” model (i.e. minimum- χ^2) out of 40 trials. Each generation up to around generation 15 (in this particular case) results in a substantial improvement in the model, seen clearly by looking at the residuals), $(D_i - M_i)/\sigma_i$, where at pixel i , D_i and M_i are the flux of the data and model respectively.

By generation 32 the models are already good, with a normalised $\chi^2 = 1.006$ at that generation. After generation 32, occasionally new components are added, and consecutive χ^2 values change only slightly. We allowed calculations to go on to generation 84 (by which time χ^2_ν has fallen to 0.897 — Section 3.6.1).

Figures 6 and 7 show the $\Delta\alpha/\alpha$ estimates for every model generated during the fitting process. In Figure 6, red and blue hollow circles illustrate the turbulent and thermal models respectively. Figure 7 (a), (b) and (c) show the best-fit models according to χ^2 -test, $AICc$ and BIC . Figure 7 (d), (e) and (f) illustrate the BMA estimates.

Table 4 gives the final estimates of $\Delta\alpha/\alpha$ for this system. The top three lines correspond to minimum values of the three statistical goodness-of-fit measures, χ^2 -test, $AICc$ and BIC , i.e. these correspond to specific models. The lower three lines give the BMA results, as described in Section 6.

Figures 6 and 7 and Table 4 illustrate three important results:

(1) The generation figure, Figure 6, shows some interesting characteristics. There is what appears to be an underlying linear trend from approximately generation 20 onwards. The most conspicuous departure from that underlying trend happens between generations 45 and 55, where $\Delta\alpha/\alpha$ rises abruptly but temporarily to a much higher value. Despite the rather dramatic change in the value of $\Delta\alpha/\alpha$ in this region, the models remain statistically good fits to the data, as Table B3 shows. Given the procedure, this feature therefore corresponds to a local minimum. In the absence of the broad picture provided by Figure 6, that is, if we were modelling the spectrum following previous methods, where only one “best fit” to the data is obtained, it would be easy to find a highly significant non-zero value of $\Delta\alpha/\alpha$. In Section 8.1 we attempt to emulate human interactive fitting and Table 5 provides some interesting quantitative information. It turns out that the $AICc$ and BIC “preferred models” (in

this emulation) fall within this generation range and hence the results are clearly anomalous. This feature and its interpretation highlight the importance of a procedure such as GVPFIT.

(2) Beyond generation 55, where the normalised χ^2_{turb} and χ^2_{therm} values had dropped to 0.998 and 0.918 respectively, the scatter reduces and a greater degree of consistency emerges for $\Delta\alpha/\alpha$ within each generation, i.e. the scatter within one generation becomes smaller than the statistical error bar.

(3) Beyond generation 55, not only does the scatter within each generation reduce, but the results become consistent across generations. $\Delta\alpha/\alpha$ is robust over a broad range of models (Table B3).

(4) Variations between the values of $\Delta\alpha/\alpha$ given in Table 4 are comfortably within the estimated statistical errors. The result for $\Delta\alpha/\alpha$ is thus insensitive to which statistic is used. Figure 7 illustrates that in this case choice of statistic is unimportant.

7.9.1 An example model

Clearly, each of the three BMA results are derived from a large number of model spectra, so we cannot easily illustrate a “best-fit” spectrum. Instead, for illustrative purposes, Figure 8 shows the minimum- $AICc$ model.

Using $AICc$, we find a minimum value occurs at $AICc_{min} = 3035$ in generation 67 (highlighted in Table B3). As expected, since BIC has a stronger penalty for increased number of free parameters and χ^2 does not penalise at all, $AICc_{min}$ falls in between the χ^2 and BIC minima.

We note again here that this model (and all others described in this paper), were derived without any human decision making other than initially defining spectral fitting ranges and identifying species detected. Initial parameter guesses were defined by the genetic algorithm and all fitting procedures are completely automated.

Figure 8 shows that the genetic algorithm has resulted in an excellent fit to the data, at least as good as could be done interactively. The residuals are well behaved and there are no discrepancies between the data and the model. The only minor exceptions are in one or two small areas where residual cosmic rays or other problems remain in the extracted spectrum (which have an insignificant impact on parameter estimation in this case). The model parameters for the fit illustrated in Figure 8 are given in Table B1.

8 COMPARISON WITH INTERACTIVE MODEL FITTING

8.1 Emulating manual fitting

Table B3 gives the statistical details for a large number of fits. For each generation, the minimum values of each of the 3 statistics used (i.e. χ^2 , $AICc$ and BIC) is given, for fully thermal or fully turbulent models. The corresponding α measurements and number of free parameters k is also shown. The total number of data points in our analysis is $n = 3258$.

We can use the data presented in Table B3 to emulate

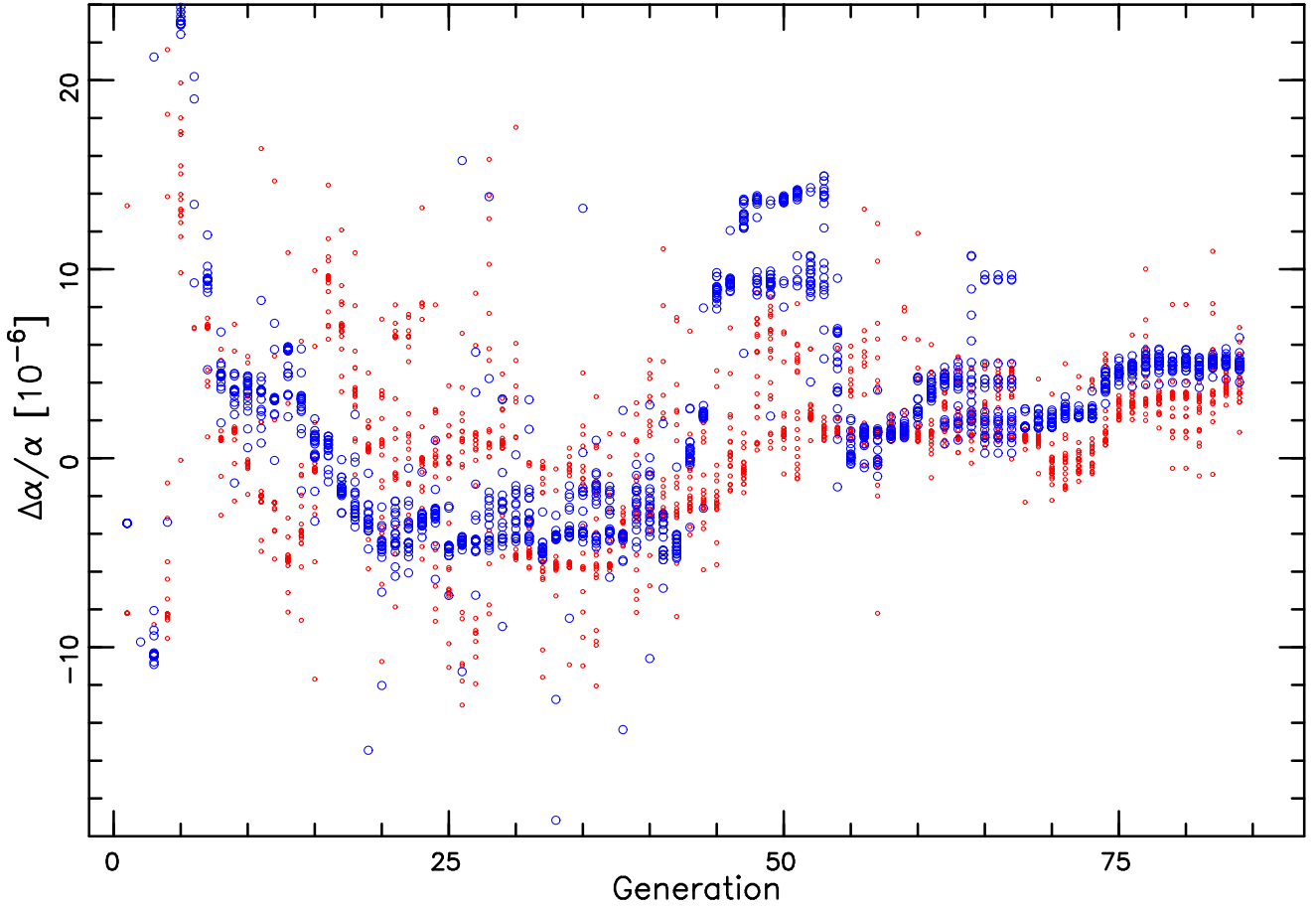


Figure 6. $\Delta\alpha/\alpha$ vs generation for all models generated during the analysis of the Fe II and Mg II absorption profiles at $z_{abs} = 1.839$ towards J110325 – 264515. The larger blue and smaller red circles show turbulent and thermal fits respectively. At increasing generation number, the models become increasingly complex. The data points suggest an underlying general trend, from which there is an abrupt departure over the generation range 43 through 55. Across this whole range, the goodness of fit (according to χ^2) is acceptable. This is clearly a local minimum in χ^2 - $\Delta\alpha/\alpha$ space, that would be impossible to identify without a thorough exploration of parameter space, but which is easily seen here. We discuss this point in detail in Section 7.9. Note that $\Delta\alpha/\alpha$ seems to stabilise to a “plateau” after approximately generation 53, where the scatter in $\Delta\alpha/\alpha$ is smaller than with the statistical uncertainty on $\Delta\alpha/\alpha$ in that region within thermal or turbulent models. The statistical uncertainties are given in Table B3 and illustrated in Figure 7.

the results that would be obtained using previous methodology i.e. a human interactively fitting the data in real-time. The emulation here is not to be considered as entirely accurate, since the way in which a human constructs models is not the same as the way in which GVPFIT constructs models. That aside, we can at least make some comparisons, bearing in mind that the usual approach used in earlier (human) analyses has been to increase the number of components in an absorption complex until the overall fit reaches a normalised χ^2 of about unity.

For the thermal model, we can see in Table B3 that $\chi^2/(n - k) \approx 1$ in generation 32. Similarly, for a turbulent model, generation 55 would be the most likely solution chosen in an interactive fit.

If instead, an interactive modeller used AICc as the preferred statistic, the likely approach would be to keep adding components to the model until both an adequate χ^2 is reached (say $\chi^2_\nu < 1.1$) and AICc increased. For the thermal models, Table B3 shows that between generation 38 and

generation 39, the AICc statistic increases (the minimum-AICc models from both generations have $\chi^2_\nu \approx 0.960$). Thus generation 38 would most likely be chosen for the thermal model. Similarly, generation 52 ($\chi^2_\nu = 1.038$) would most likely be chosen for the best turbulent model.

Using the BIC statistic (although to our knowledge BIC has not been used in this context before), Table B3 shows that the chosen thermal model would be generation 33 ($\chi^2_\nu = 0.992$) and the turbulent model would be generation 47 ($\chi^2_\nu = 1.068$).

Accepting the shortcomings of this comparison, a human (using AICc) would therefore probably select the solutions in generations 52 (turbulent) or 38 (thermal). In contrast, as can be seen in Table 4, GVPFIT would select generation 79. Table 5 summarises the values above, with the corresponding values of $\Delta\alpha/\alpha$. Emulating the “usual” human interactive fitting procedure clearly results in selecting models with fewer free parameters ($k = 132$ -137, 140-148 and 121-124 when using χ^2 , AICc and BIC respectively)

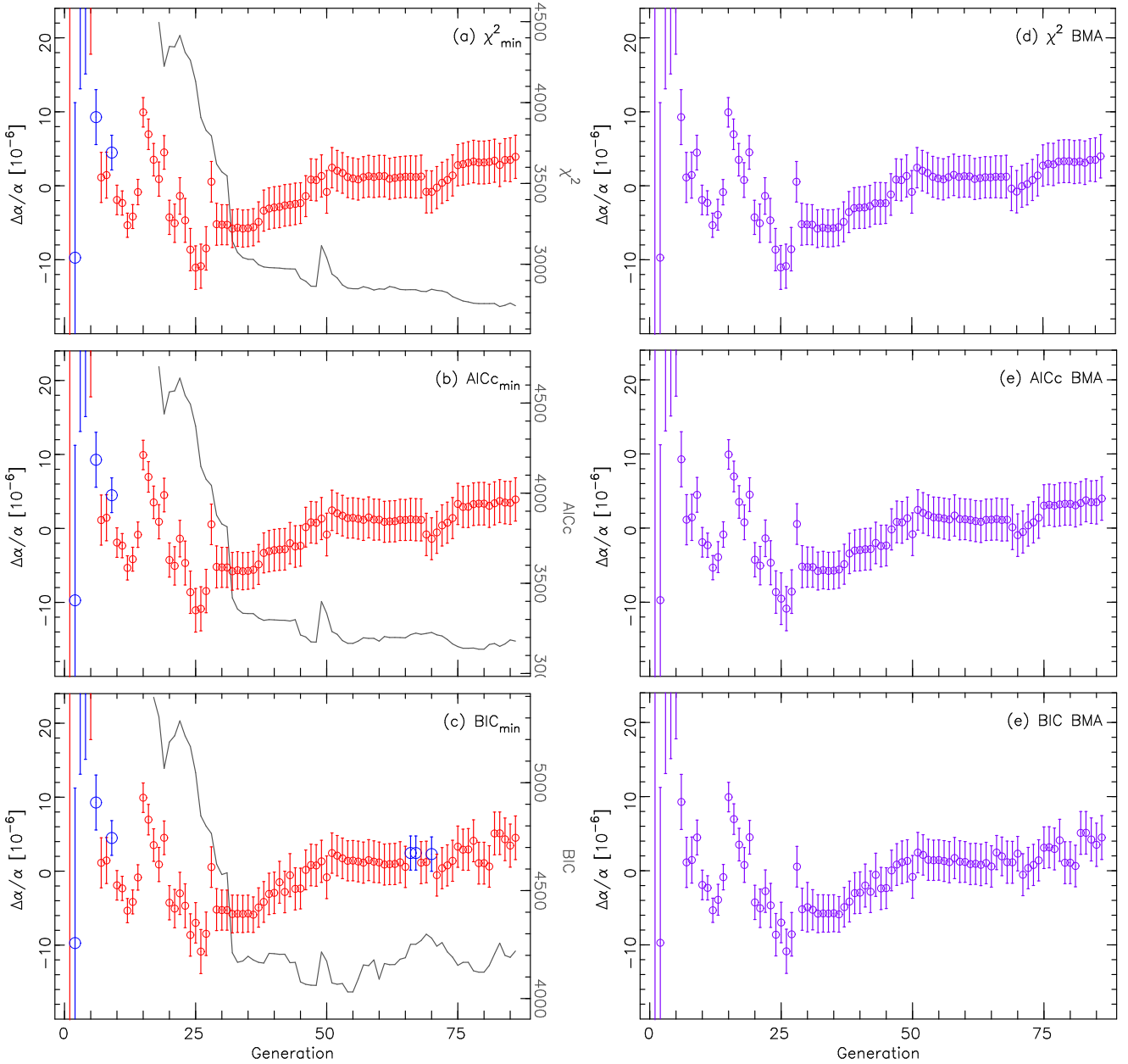


Figure 7. Comparison of $\Delta\alpha/\alpha$ evolution for different methods of analysis. Left-hand panels (a), (b), and (c): Each point in these 3 panels corresponds to the $\Delta\alpha/\alpha$ estimate of the model with a minimum in each statistic (χ^2 , AICc and BIC respectively) from the combined set of thermal and turbulent models for that generation. Again, larger blue and smaller red circles show turbulent and thermal fits respectively. After generation 10 the thermal models are preferred over turbulent models, with only a few exceptions, in all three statistics (χ^2 , AICc and BIC). The continuous grey line illustrates the value of the statistic itself. The features or spikes in the grey line are present because we plot the absolute (as opposed to the normalised) value of the statistic, and the number of free parameters in the fit is fluctuating slightly between competing models. Right-hand panels (d), (e), and (f): Each point in these 3 panels corresponds to the BMA $\Delta\alpha/\alpha$ estimate for that generation, using the relevant statistic (χ^2 , AICc and BIC respectively). In all panels, error bars illustrate statistical uncertainties, derived from the diagonal of the covariance matrix in VPFIT.

compared to models selected using the same statistics after applying GVPFIT. Table B3 shows that the three non-BMA values in Table 4 have global minima at much higher complexity, generations 83, 79 and 55 for χ^2_{min} ($k = 198$), $AICc_{min}$ ($k = 176$) and BIC_{min} ($k = 144$) respectively.

Of particular importance in this “human emulation” attempt, are the $\Delta\alpha/\alpha$ results revealed in Table 5. Using established statistical selection criteria, AICc and BIC, we

happen to end up in a local minimum in parameter space that produces an anomalous result for $\Delta\alpha/\alpha$ yet provides a statistically good fit to the data. We discuss this local minimum more detail in Section 7.9 and note here that the GVPFIT procedure provides a “global picture”, enabling the anomalous region to be clearly seen. We thus argue that GVPFIT outperforms any human interactive modeller in this respect.

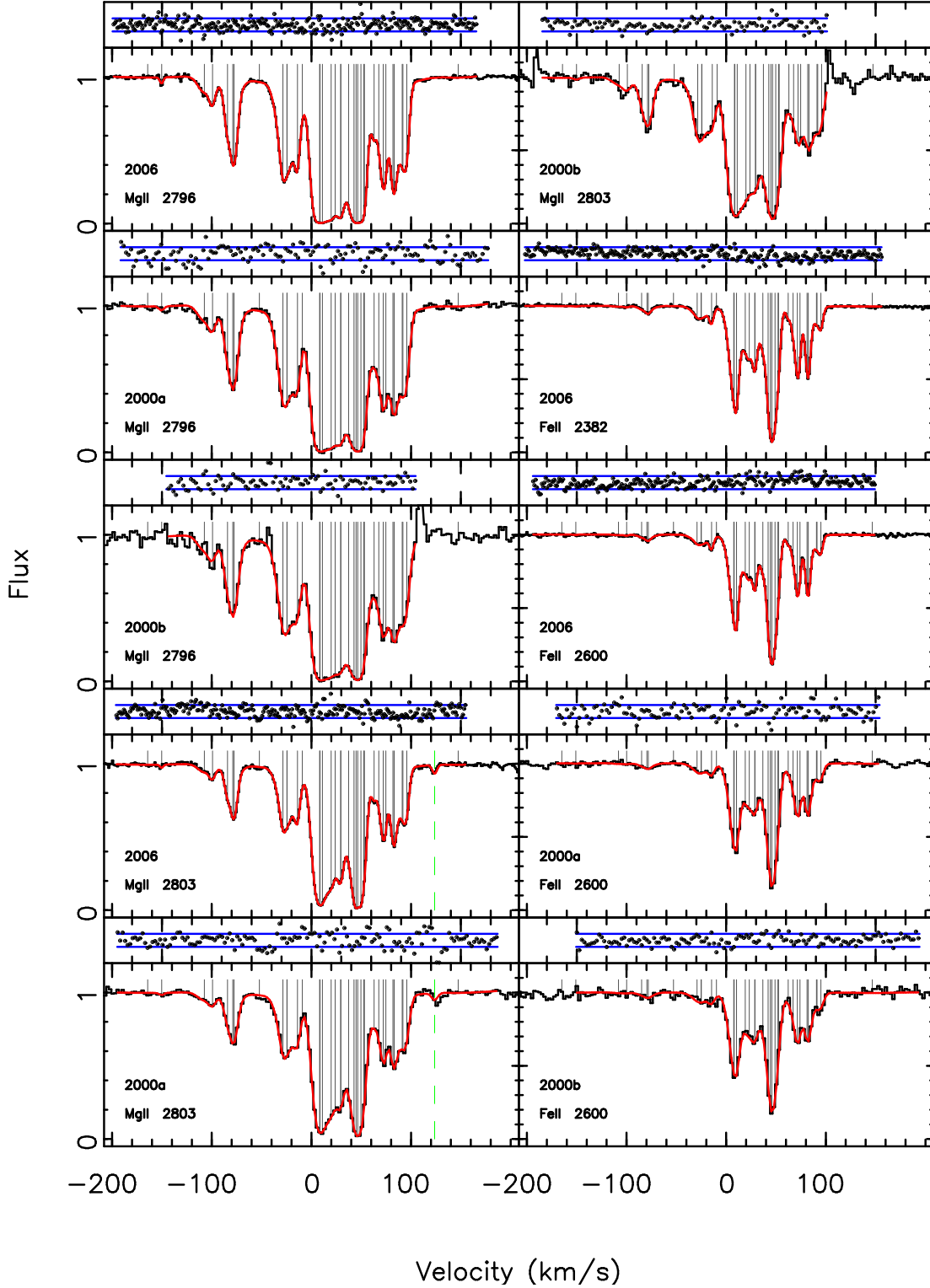


Figure 8. Comparison of the minimum- AIC_c model and the spectral data. There are two panels on each row: the top panel compares the residuals (black points) to the 1σ expected fluctuations (horizontal blue lines). The bottom panel compares the minimum- AIC_c model (smooth red line) to the data (black). Each velocity component is shown as a grey vertical line. Vertical dashed (green) lines indicate interlopers (i.e. additional components assumed to be from some other species at some other redshifts).

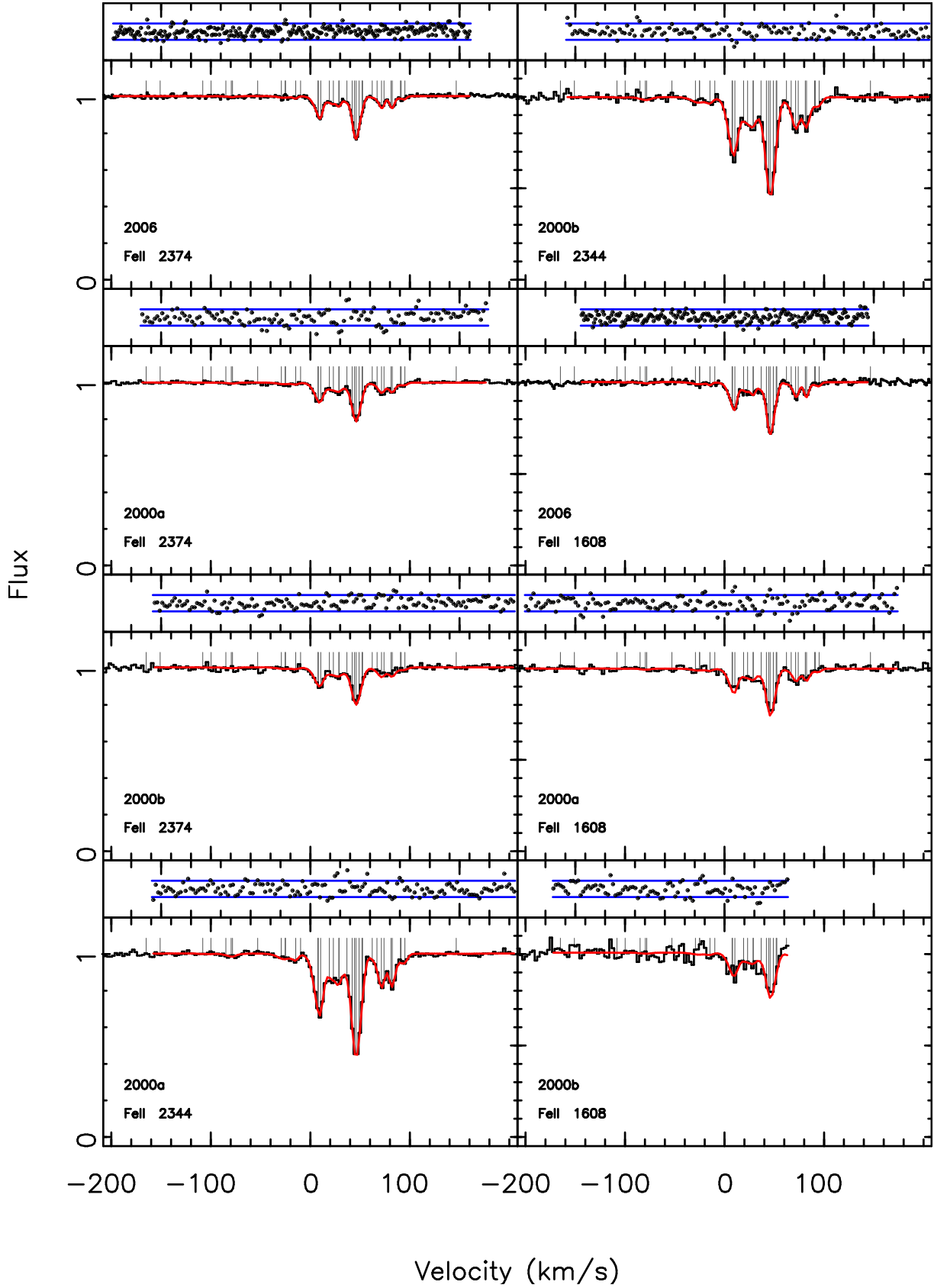


Figure 8 – *continued*. Comparison of the minimum- $AICc$ model and the spectral data.

Table 4. Comparison of final $\Delta\alpha/\alpha$ estimates by statistical criteria. Each statistical criteria is used to analyse the set of candidate models and estimate a single $\Delta\alpha/\alpha$ value. Row 1: minimum χ^2 model. Row 2: minimum Akaike Information Criteria corrected for small sample size ($AICc$) model. Row 3: minimum Bayesian Information Criteria (BIC) model. These three models correspond to the minimum in the respective statistic when the entire set of thermal and turbulent models are compared. The three models, in this case, are thermally broadened and highlighted in Table B3; χ^2_{min} generation 83 ($k = 198$), $AICc_{min}$ generation 79 ($k = 176$), and BIC_{min} generation 55 ($k = 144$), respectively. Row 4, 5 and 6: Bayesian Model Averaging (BMA), applied to the combined set of all thermal and turbulent models, using the χ^2 , $AICc$ and BIC statistics, respectively. See Section 6 for a discussion of BMA

Source	$\Delta\alpha/\alpha$ [10^{-6}]
χ^2_{min}	2.8 ± 2.9
$AICc_{min}$	3.3 ± 2.9
BIC_{min}	1.4 ± 2.7
χ^2 , BMA	3.2 ± 3.0
$AICc$, BMA	3.3 ± 2.9
BIC , BMA	1.4 ± 2.7

Table 5. $\Delta\alpha/\alpha$ results from emulating human interactive fitting. Here we treat the thermal and turbulent cases separately, as has been done in many previous analyses of $\Delta\alpha/\alpha$. To emulate a human interactive fit, we use three statistical measures and select a "preferred model" from Table B3 in each case. See Section 8.1 for more information. Column 1: statistical criteria used in the fitting process. Column 3: model generation, from Table B3. Column 4: number of free parameters in the model.

Statistic		Gen.	k	$\Delta\alpha/\alpha$ [10^{-6}]
χ^2_{min}	(thermal)	32	132	-5.8 ± 2.6
$AICc_{min}$	(thermal)	38	148	-3.3 ± 2.7
BIC_{min}	(thermal)	33	124	-5.8 ± 2.5
χ^2_{min}	(turbulent)	55	137	1.1 ± 1.8
$AICc_{min}$	(turbulent)	52	140	14.1 ± 2.2
BIC_{min}	(turbulent)	47	121	13.7 ± 1.9

8.2 Comparison with previous results for the $z_{abs} = 1.839$ absorption system towards J110325-264515

Table 6 compares our AICc BMA result with the results from 5 previous studies of the same absorption system. Note that none of the results given in Table 6 can be considered independent since the data used have at least some commonality in all analyses listed.

Our minimum-AICc model is also included in Table 6, for completeness and so that we can compare χ^2 values, number of velocity components, and number of data points used in each analysis.

When comparing a spectral range common to all analyses including this new one (see Table 6), our minimum-AICc model has 14 components. Previous analyses have between 6 and 15 components in that same range. We have used a somewhat larger dataset in the present analysis, incorporating observations over many years (Table 2) so our overall signal-to-noise ratio is somewhat higher. We have also included MgII whereas none of the previous analyses did. It is therefore unsurprising that the number of components in

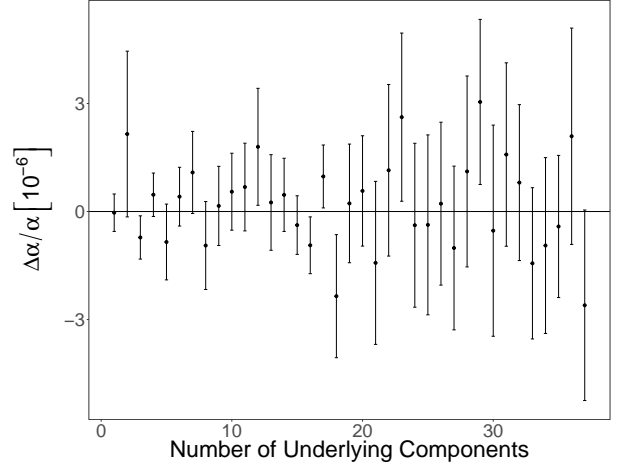


Figure 9. $\Delta\alpha/\alpha$ vs number of velocity components for the set of synthetic spectra described in Section 9. We created 37 synthetic spectra whose parameters were drawn from the minimum-AICc models for the $z_{abs} = 1.839$ system towards J110325-264515 for models that contained 1, 2, 3,...,37 velocity components. $\Delta\alpha/\alpha$ is set to zero in these simulations. The results illustrated here show the BMA results of applying GVPFIT to all 37 synthetic spectra. The 1σ statistical uncertainties are derived in the same way as for the real data. As can be seen GVPFIT recovers the input $\Delta\alpha/\alpha$ value within the expected statistical uncertainty.

our AICc model is relatively high. We note that the King et al. (2012) model uses only 9 components yet also has used AICc to select the most appropriate model.

8.3 Apparent over-fitting

Careful inspection of Figure 8 may suggest too many parameters have been used to model the data. For example, looking at the top left panel for MgII 2796 (where the signal-to-noise is high), there are 3 cases of very close blends. An experienced "manual-fitter" may intuitively regard this as over-fitting. However, in fact, in all 3 cases, the close pairs of blends have significantly different b -parameters, so contribute quite differently to the profile shape. The model presented in Figure 8 is not intended to represent a definitive model for this absorption system. Nevertheless, it is the minimum AICc model, the procedure is objective and reproducible, the normalised residuals obtained for the fit are good, and BMA in any case downplays the importance of any specific model.

9 TESTING GVPFIT USING SYNTHETIC SPECTRA

In Section 4 we described some relatively simple simulations that served to illustrate how GVPFIT works and also as a basic test. In this Section we describe simulations of spectra with a broad range of velocity structures, ranging from extremely simple up to highly complex. The simulations described in this Section are based on the characteristics of the real absorption system analysed in Section 7.

Table 6. Comparison to Previously Published Models. Column 2: This work’s *AICc* BMA estimate, Column 3: This work’s minimum-*AICc* model, Column 4: Levshakov et al. (2005), Column 5: Levshakov et al. (2007), Column 6: Molaro et al. (2008), Column 7: Levshakov et al. (2009), Column 8: King et al. (2012). Row 1: $\Delta\alpha/\alpha$ in units of 10^{-6} , Row 2: normalised χ^2 , Row 3: number of data points, Row 5: number of velocity components between -50 km/s and 40 km/s (the common velocity range in the models).

	This Work <i>AICc</i> BMA	This Work Minimum- <i>AICc</i> Model	Levshakov 2005	Levshakov 2007	Molaro 2008	Levshakov 2009	King 2012
$\Delta\alpha/\alpha$	3.3 ± 2.9		2.4 ± 3.8	5.4 ± 2.5	5.7 ± 2.7	4.0 ± 2.8	6.1 ± 4.0
χ^2_ν		0.896	1.097	0.901	0.90	0.87	0.935
n	3258	3258	973	306	—	352	388
n_{comp}		14	6	11	11	15	9

— information unavailable from publication.

From the whole database created when running GVPFIT on the real spectra, we selected the minimum-*AICc* model with 1 through 37 velocity components. The best-fit parameters from these 37 models were then used to create 37 model spectra. We go up to 37 because a 37-component fit corresponds to the minimum-*AICc* model for the real data.

Synthetic models were created directly from the appropriate VPFIT output, hence were convolved with the same instrumental profile as used in fitting the real spectra. Gaussian noise was added to each model using the Box-Muller transform approach (Box & Muller 1958). We used the actual error arrays from the real spectra to assign Gaussian standard deviation at each pixel in each synthetic spectrum created, thus emulating the characteristics of the real data closely. The real spectra have multiple observations from different epochs. Synthetic spectra corresponding to each of the real spectra were created. The synthetic spectra were created and fitted using turbulent b-parameters only. The calculations were not repeated for thermal models. This is a minor difference between the treatment of the simulations compared to the real data but this has no relevance in terms the usefulness of these simulations as a stringent test of GVPFIT.

We then treated the synthetic spectra described above as if they were real data, applied GVPFIT to each of these 37 models and *AICc* BMA values for $\Delta\alpha/\alpha$, as described in Section 7.9. The 37 results are illustrated in Figure 9. Error bars grow as the absorption system complexity increases, as would be expected. The weighted mean over the 37 values of $\Delta\alpha/\alpha$ is $0.04 \pm 0.20 \times 10^{-6}$ and no bias for the $\Delta\alpha/\alpha$ estimate is seen.

The simulation results provide additional informative performance details. The set of input models comprises $\sum_{i=1}^{37} n_i = 703$ components, where n_i is the number of velocity components for the i^{th} model. In other words, if GVPFIT was a perfect procedure, it should have detected exactly 703 components in total for the entire set of simulations.

As a test of this, we compared the 37 minimum-*AICc* models from the simulations with the input models. We found that 653 of the 703 real velocity components were successfully identified. Also, 4 additional velocity components were introduced in the GVPFIT fitting process that were not present in the original models. GVPFIT therefore successfully identified 92.9% of the real components present and only 0.6% of spurious velocity components were introduced.

We summarise the outcome of these simulations with two conclusions: (1) Using realistic simulated spectra covering a broad range in complexity, GVPFIT returns results

that are accurate and unbiased; (2) A second interesting implication is that selecting the minimum-*AICc* does a good job in selecting the “right” model, with no evidence for over- or under-fitting.

10 CONCLUSIONS

(1) We have introduced Genetic Voigt Profile FIT (GVPFIT), a new “artificial intelligence” genetic algorithm for the analysis of absorption spectra (in quasars, the interstellar medium, or stellar astrophysics).

(2) Using this genetic algorithm we present a new method for the analysis of absorption spectra. The method is memetic, unifying a genetic algorithm (GVPFIT), non-linear least-squares optimisation (VPFIT), and Bayesian Model Averaging (BMA). In contrast to previous methodologies, BMA derives results using a large set of models, providing a more robust final answer compared to picking a single preferred model since it avoids the systematic uncertainties associated with model choice. This new method eliminates most of the human decision-making processes and hence minimises or removes any possible bias.

(3) Robust and automated $\Delta\alpha/\alpha$ estimation permits a more complete analysis (i.e. a large set of models rather than just a single model). Since GVPFIT provides a “global view” over many generations (i.e. complexities) and we can identify local minima. This may apply to other “interesting” parameters, not only $\Delta\alpha/\alpha$. GVPFIT out-performs human interactive fitting in this respect.

(4) We have applied GVPFIT to the measurement of the fine structure constant in a high-redshift quasar absorption system, at $z_{\text{abs}} = 1.839$, towards the quasar J110325-264515. The result is consistent both with zero and with the tentative spatial variation of α reported in Webb et al. (2011) and King et al. (2012).

(5) We find that sets of statistically acceptable models can be found which nonetheless are anomalous in terms of $\Delta\alpha/\alpha$. A human interactive fitting process could not easily identify these regions, whereas GVPFIT can.

(6) Comparing GVPFIT with emulations of previous interactive fitting methods, which require far more human decision-making, we see that GVPFIT provides greater consistency and stability (Tables 4, 5, 6 and associated discussion).

(7) Since the human-work in modelling absorption spectra is now removed by GVPFIT, future projects that were previously unrealistic are now feasible. One example of this

is modelling both thermal and turbulent models for each absorption system independently, allowing a more reliable comparison between models and data. This analysis has been done for the first time here (applied to the $z_{abs} = 1.839$ absorption system towards the quasar J110325-264515).

ACKNOWLEDGEMENTS

We would like to thank Bob Carswell. Much of the content of this paper is built upon our collaborative work over many years. We thank Signe Riemer-Sørensen, Michael Wilczynska and Evgeny Zavarygin for detailed comments, Vincent Dumont for discussions about atomic data, and Michael Murphy for communications regarding initial data reduction and for comments on an early draft. We also are grateful to Adrian Raftery and Jennifer Hoeting for input concerning BMA, and to referee, Ewan Cameron, for his detailed criticisms, which we think resulted in a much improved paper. MBB is grateful for postgraduate scholarship support from UNSW.

REFERENCES

- Adriaan van den Bos 2007, *Parameter Estimation for Scientists and Engineers*. Wiley
- Akaike H., 1973, in Petrov B. N., Csaki F., eds, *Second international symposium on information theory Information theory and an extension of the maximum likelihood principle*. Budapest, Hungary, pp 267–281
- Ansbacher W., Li Y., Pinnington E. H., 1989, *Physics Letters A*, 139, 165
- Audi G., Wapstra A. H., Thibault C., 2003, *Nucl. Phys. A*, 729, 337
- Batteiger V., Knünz S., Herrmann M., Saathoff G., Schüssler H. A., Bernhardt B., Wilken T., Holzwarth R., Hänsch T. W., Udem T., 2009, *PRA*, 80, 022503
- Berengut J. C., Dzuba V. A., Flambaum V. V., King J. A., Kozlov M. G., Murphy M. T., Webb J. K., 2011, *Atomic Transition Frequencies, Isotope Shifts, and Sensitivity to Variation of the Fine Structure Constant for Studies of Quasar Absorption Spectra*. Springer, Springer-Verlag Berlin Heidelberg, p. 9
- Bergeson S. D., Mullman K. L., Lawler J. E., 1996, *APJ*, 464, 1050
- Bergeson S. D., Mullman K. L., Wickliffe W. E., Lawler J. E., Litzen U., Johansson S., 1996, *APJ*, 464, 1044
- Biemont E., Baudoux M., Kurucz R. L., Ansbacher W., Pinnington E. H., 1991, *AAP*, 249, 539
- Box G. E. P., Muller M. E., 1958, *The Annals of Mathematical Statistics*, 29, 610
- Bozdogan H., 1987, *Psychometrika*, 52, 345
- Carswell R. F., Lanzetta K. M., Parnell H. C., Webb J. K., 1991, *Mon. Not. Roy. Astron. Soc.*, 371, 36
- Carswell R. F., Morton D. C., Smith M. G., Stockton A. N., Turnshek D. A., Weymann R. J., 1984, *Mon. Not. Roy. Astron. Soc.*, 278, 486
- Carswell R. F., Webb J. K., 2015, *VPFIT*, Voigt profile fitting program – <http://www.ast.cam.ac.uk/~rfc/vpfit.html>
- Carswell R. F., Whelan J. J. A., Smith M. G., Boksenberg A., Tytler D., 1982, *Mon. Not. Roy. Astron. Soc.*, 198, 91
- Dekker H., D’Odorico S., Kaufer A., Delabre B., Kotzlowski H., 2000, in Iye M., Moorwood A. F., eds, *Optical and IR Telescope Instrumentation and Detectors Vol. 4008 of Society of Photo-Optical Instrumentation Engineers (SPIE) Conference Series, Design, construction, and performance of UVES, the echelle spectrograph for the UT2 Kueyen Telescope at the ESO Paranal Observatory*. pp 534–545
- Draper D., 1995, *J. R. Statist. Soc. B*, 1, 45
- Dzuba V. A., Flambaum V. V., Kozlov M. G., Marchenko M., 2002, *PRA*, 66, 022501
- Dzuba V. A., Johnson W. R., 2007, *PRA*, 76, 062510
- Gill P. E., Murray W., Wright M. H., 1981, *Practical Optimization*. Academic Press Inc. Harcourt Brace Jovanovich Publishers, London
- Godefroid M., Froese Fischer C., 1999, *Journal of Physics B Atomic Molecular Physics*, 32, 4467
- Hodges J. S., 1987, *Statist. Sci.*, 2, 259
- Hoeting J. A., Madigan D., Raftery A. E., Volinsky C., 1999, *Statist. Sci.*, 14, 382
- Holland J. H., 1975, *Adaptation in Natural and Artificial Systems*. University of Michigan Press
- Hurvich C. M., Tsai C.-L., 1989, *Biometrika*, 76, 297
- Itano W. M., Wineland D. J., 1981, *PRA*, 24, 1364
- Kaufman V., Martin W. C., 1991, *Journal of Physical and Chemical Reference Data*, 20, 83
- King J. A., Mortlock D. J., Webb J. K., Murphy M. T., 2009a, *Mem. Soc. Astron. Ital.*, 80, 864
- King J. A., Mortlock D. J., Webb J. K., Murphy M. T., 2009b, *Memorie della Società Astronomica Italiana*, 80, 864
- King J. A., Webb J. K., Murphy M. T., Flambaum V. V., Carswell R. F., Bainbridge M. B., Wilczynska M. R., Koch F. E., 2012, *MNRAS*, 422, 3370
- Krasnogor N., 2010, *Handbook of Natural Computation*. Springer Berlin / Heidelberg, p. t.a.
- Larsen J. M., Modigliani A., Bramich D., 2015, *UVES_PIPELINE*
- Leamer E. E., 1978, *Specification Searches*. Wiley, New York
- Levshakov S. A., Agafonova I. I., Molaro P., Reimers D., Hou J. L., 2009, *AAP*, 507, 209
- Levshakov S. A., Centurión M., Molaro P., D’Odorico S., 2005, *AAP*, 434, 827
- Levshakov S. A., Molaro P., Lopez S., D’Odorico S., Centurión M., Bonifacio P., Agafonova I. I., Reimers D., 2007, *AAP*, 466, 1077
- Li Z. S., Lundberg H., Berzinsh U., Johansson S., Svanberg S., 2000, *Journal of Physics B Atomic Molecular Physics*, 33, 5593
- Molaro P., Reimers D., Agafonova I. I., Levshakov S. A., 2008, *European Physical Journal Special Topics*, 163, 173
- Murphy M. T., 2010, *UVES_POPLER* – http://astronomy.swin.edu.au/~mmurphy/UVES_popler
- Murphy M. T., Webb J. K., Flambaum V. V., 2007, *Phys. Rev. Lett.*, 99, 239001
- Nave G., 2012, *MNRAS*, 420, 1570
- Osmer P. S., Smith M. G., 1977, *Mon. Not. Roy. Astron. Soc.*, 213, 607
- Porsev S. G., Koshelev K. V., Tupitsyn I. I., Kozlov M. G., Reimers D., Levshakov S. A., 2007, *PRA*, 76, 052507
- Porsev S. G., Kozlov M. G., Reimers D., 2009, *PRA*, 79, 032519
- Raftery A. E., Madigan D., Hoeting J. A. J., 1997, *Amer. Statist. Assoc.*, 92, 179
- Riemer-Sørensen S., Webb J. K., Crighton N., Dumont V., Ali K., Kotuš S., Bainbridge M., Murphy M. T., Carswell R., 2015, *MNRAS*, 447, 2925
- Rosman K. J. R., Taylor P. D. P., 1998, *Journal of Physical and Chemical Reference Data*, 27, 1275
- Spall J. C., 2003, *Introduction to Stochastic Search and Optimization: Estimation, Simulation, and Control*. Wiley
- Sudholt D., 2009, *Theor. Comput. Sci.*, 410, 2511
- Sur C., Sahoo B. K., Chaudhuri R. K., Das B. P., Mukherjee D., 2005, *European Physical Journal D*, 32, 25
- Taylor P. D. P., Maeck R., de Bièvre P., 1992, *Int. J. Mass Spectrom.*, 121, 111
- Webb J. K., King J. A., Murphy M. T., Flambaum V. V., Carswell

- R. F., Bainbridge M. B., 2011, Physical Review Letters, 107, 191101
- Wilczynska M. R., Webb J. K., King J. A., Murphy M. T., Bainbridge M. B., Flambaum V. V., 2015, MNRAS, 454, 3082
- Winker P., Gilli M., 2004, Computational Statistics and Data Analysis, 47, 211
- Worden E. F., Comaskey B., Densberger J., Christensen J., McAfee J. M., Paisner J. A., Conway J. G., 1984, Journal of the Optical Society of America B Optical Physics, 1, 314

APPENDIX A: ATOMIC DATA

Here we provide details for the MgII and FeII atomic data used in our analysis. The transitions used in this work are identified in Table A1. The characteristics and Voigt profile parameters for these transitions are given in Table A2.

A1 MgII 2796/2803Å hyperfine transitions

The MgII hyperfine structure results from the interaction of the nuclear electric and magnetic fields with the electron angular momentum and spin. It impacts those isotopes with a non-zero nuclear spin which are thus themselves split further. Hyperfine splitting occurs to both the lower and upper levels of a transition, although the effect on the lower level dominates and the upper level splitting is often not considered.

The $^{25}\text{MgII}$ isotope is split into the twelve hyperfine transitions (illustrated in Figure A1), whose wavenumbers can be calculated from the magnetic dipole hyperfine constants, A_i and A_j , and the electric quadrupole hyperfine constant, B

$$\omega_{25}^{i,j} = \omega_{24} + \Delta\omega_{24,25} + \frac{1}{2} [A^i K^i + A^j K^j + BC^j] \quad (\text{A1})$$

where $\omega_{25}^{i,j}$ is the wavenumber for the hyperfine transition from the i^{th} lower level to the j^{th} upper level, $\Delta\omega_{24,25}$ is the wavenumber shift between $^{24}\text{MgII}$ and the observed centroid for $^{25}\text{MgII}$, and K is given by

$$K = F(F+1) - J(J+1) - I(I+1) \quad (\text{A2})$$

and C is

$$C = \frac{3K(K+1) - 4(I+1)J(J+1)}{2I(2I-1)2J(2J-1)} \quad (\text{A3})$$

where $F = |I+J|$, I is the nuclear angular momentum and J is the electron angular momentum. The uncertainty on the $^{25}\text{MgII}$ hyperfine wavenumbers are given by the centroid uncertainties i.e.

$$\sigma\omega_{25}^{i,j} \approx \Delta\omega_{24} \quad (\text{A4})$$

The $^{25}\text{MgII}$ hyperfine structures abundances are taken to be equally populated, under the assumption of local thermodynamic equilibrium at the cosmic microwave background temperature (i.e. $\frac{N_i}{N_j} = \frac{g_i}{g_j} e^{-\Delta E_{i,j}/kT} \approx 1$).

The details of the MgII hyperfine structure are given in Table A3. The MgII vacuum wavelengths, λ_{vac} and wavenumbers, $\omega = f/c$, where f is the frequency and c is the speed of light in a vacuum, and their associated uncertainties, are given in Table A6.

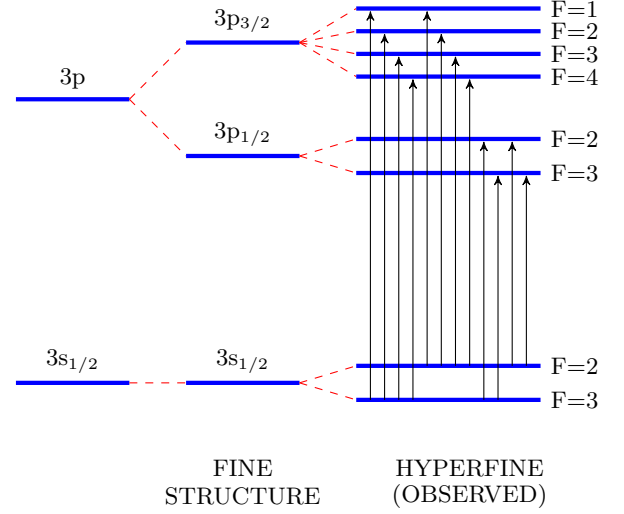


Figure A1 – Energy level diagram for observed $^{25}\text{MgII}$ hyperfine transitions. Ordering of transitions, from left to right, is in ascending wavelength, as in Table A3.

A2 FeII

We have used slightly different wavelengths to those in King et al. (2012) since newer FeII laboratory (centroid) wavelengths are available from Nave (2012).

The frequency shift, $\delta\omega^{A,A'}$, between the transitions of two isotopes with mass numbers A and A' can be approximated, by neglecting the field shift, as shown in (Porsev et al. 2009)

$$\delta\omega^{A,A'} = \omega^A - \omega^{A'} \approx k_{\text{MS}} \left\{ \frac{1}{A} - \frac{1}{A'} \right\} \quad (\text{A5})$$

where k_{MS} is the total mass shift given in Table A5 and the mass numbers are given in A4.

In addition we can relate the frequencies of the isotopes of FeII to the observed centroid frequency, ω , assuming terrestrial isotopic abundance,

$$\omega = \omega^{54} P^{54} + \omega^{56} P^{56} + \omega^{57} P^{57} + \omega^{58} P^{58} \quad (\text{A6})$$

where P^A is the terrestrial isotopic abundance of the isotope with mass number A , shown in Table A6 as Relative Strength.

Combining Equations A5 and A6 we solved for the frequency of the FeII 54 transitions, and from that frequency the remaining isotopic structure as shown in Table A6.

Table A1. Atomic Data – Transition Classification. Column 1 and 2: atomic species^[2] and transition label^[2], Column 3 and 4: lower and upper atomic state electronic configurations. The superscripts, e.g. ^[3], correspond to the list of references given in Table A7.

Species	Tran.	Lower State	Upper State
Fe II	1608	$3d^6(^5D)4sa^6D_{9/2}^{[3]}$	$3d^5(^6S)4s4p(^3P)y^6P_{7/2}^o^{[3]}$
Fe II	2344	$3d^6(^5D)4sa^6D_{9/2}^{[3]}$	$3d^6(^5D)4pz^6P_{7/2}^o^{[3]}$
Fe II	2374	$3d^6(^5D)4sa^6D_{9/2}^{[3]}$	$3d^6(^5D)4pz^6F_{9/2}^o^{[3]}$
Fe II	2382	$3d^6(^5D)4sa^6D_{9/2}^{[3]}$	$3d^6(^5D)4pz^6F_{11/2}^o^{[3]}$
Fe II	2586	$3d^6(^5D)4sa^6D_{9/2}^{[3]}$	$3d^6(^5D)4pz^6D_{7/2}^o^{[3]}$
Fe II	2600	$3d^6(^5D)4sa^6D_{9/2}^{[3]}$	$3d^6(^5D)4pz^6D_{9/2}^o^{[3]}$
Mg II	2796	$3s^2S_{1/2}^{[16]}$	$3p^2P_{3/2}^{[16]}$
Mg II	2803	$3s^2S_{1/2}^{[16]}$	$3p^2P_{1/2}^{[16]}$

Table A2. Atomic Data – Voigt Profile Parameters. The rest wavelengths are shown in Table A6. Column 1 and 2: atomic species and transition^[2]. Column 3: atomic mass. Column 4 and 5: lower and upper ionisation potentials. Column 6: oscillator strength of the centroid. Column 7: energy level lifetime. Column 8: centroid transition dampening constant. Column 9: q -coefficient (uncertainties as in Berengut et al. (2011)). The superscripts, e.g. ^[3], correspond to the list of references given in Table A7.

Species	Tran.	Atomic Mass [amu]	Lower IP [eV]	Upper IP [eV]	f	τ [ns]	Γ [10 ⁸ s ⁻¹]	q [cm ⁻¹]
Fe II	1608	55.845(19) ^[4]	7.9024(1) ^[7]	16.19920(5) ^[3]	0.058(5) ^[8]	3.65(20) ^[10]	2.74(15) ^[26]	-1165(300) ^[12,13]
Fe II	2344				0.114(2) ^[9]	3.73(5) ^[11]	2.68(4) ^[26]	1375(300) ^[12,13]
Fe II	2374				0.0313(14) ^[9]	3.24(6) ^[11]	3.09(6) ^[26]	1625(100) ^[12,13]
Fe II	2382				0.320(4) ^[9]	3.19(4) ^[11]	3.13(4) ^[26]	1505(100) ^[12,13]
Fe II	2586				0.0691(25) ^[9]	3.68(7) ^[11]	2.72(5) ^[26]	1515(100) ^[12,13]
Fe II	2600				0.239(4) ^[9]	3.70(6) ^[11]	2.70(4) ^[26]	1370(100) ^[12,13]
Mg II	2796	24.3051(53) ^[4]	7.646238(5) ^[19]	15.035277(8) ^[19]	0.611(2) ^[20]	3.854(30) ^[21]	2.595(20) ^[26]	212(1) ^[22]
Mg II	2803				0.306(5) ^[20]	3.810(40) ^[21]	2.625(28) ^[26]	121(1) ^[22]

Table A3. Atomic Data – MgII 25 Hyperfine Structure. For this atom $I = 5/2$. Columns 2 and 5: atomic configuration. Columns 3 and 6: electron angular momentum. Columns 4 and 7: magnitude of the F quantum number, which is the vector sum of the total angular momentum for the nuclear state and electron state. Column 8: isotopic shift from the ²⁴MgII centroid to the ²⁵MgII centroid energy levels, Column 9 and 10: magnetic dipole hyperfine constant, for the i^{th} and j^{th} state, respectively. Column 11: electric dipole hyperfine constant for the j^{th} state. Column 12: i^{th} energy level. Column 13: j^{th} energy level. The superscripts, e.g. ^[3], correspond to the list of references given in Table A7.

#	Lower State ^[16]	\mathbf{J}^i	F^i	Upper State ^[16]	\mathbf{J}^j	F^j	$\Delta\omega_{24,25}$ ^[16] (10 ⁻²) [cm ⁻¹]	A^i ^[25] (10 ⁻²) [cm ⁻¹]	A^j ^[28] (10 ⁻⁴) [cm ⁻¹]	B^j ^[28] (10 ⁻⁴) [cm ⁻¹]	E^i (10 ⁻²) [cm ⁻¹]	E^j [cm ⁻¹]
1	3s ² S _{1/2}	1/2	3	3p ² P _{3/2}	-3/2	1	5.407(63)	-1.98889051(18)	-0.6301	-0.7642	-2.48611314(23)	35760.8940400(53)
2	3s ² S _{1/2}	1/2	3	3p ² P _{3/2}	-1/2	2	5.407(63)	-1.98889051(18)	-0.6301	-0.7642	-2.48611314(23)	35760.8925701(53)
3	3s ² S _{1/2}	1/2	3	3p ² P _{3/2}	1/2	3	5.407(63)	-1.98889051(18)	-0.6301	-0.7642	-2.48611314(23)	35760.8906798(53)
4	3s ² S _{1/2}	1/2	3	3p ² P _{3/2}	3/2	4	5.407(63)	-1.98889051(18)	-0.6301	-0.7642	-2.48611314(23)	35760.8889135(53)
5	3s ² S _{1/2}	-1/2	2	3p ² P _{3/2}	-3/2	1	5.407(63)	-1.98889051(18)	-0.6301	-0.7642	3.48055840(32)	35760.8940400(53)
6	3s ² S _{1/2}	-1/2	2	3p ² P _{3/2}	-1/2	2	5.407(63)	-1.98889051(18)	-0.6301	-0.7642	3.48055840(32)	35760.8925701(53)
7	3s ² S _{1/2}	-1/2	2	3p ² P _{3/2}	1/2	3	5.407(63)	-1.98889051(18)	-0.6301	-0.7642	3.48055840(32)	35760.8906798(53)
8	3s ² S _{1/2}	-1/2	2	3p ² P _{3/2}	3/2	4	5.407(63)	-1.98889051(18)	-0.6301	-0.7642	3.48055840(32)	35760.8889135(53)
9	3s ² S _{1/2}	1/2	3	3p ² P _{1/2}	-1/2	2	5.404(63)	-1.98889051(18)	-3.3923	N/A	-2.48611314(23)	35669.3476437(53)
10	3s ² S _{1/2}	1/2	3	3p ² P _{1/2}	1/2	3	5.404(63)	-1.98889051(18)	-3.3923	N/A	-2.48611314(23)	35669.3374666(53)
11	3s ² S _{1/2}	-1/2	2	3p ² P _{1/2}	-1/2	2	5.404(63)	-1.98889051(18)	-3.3923	N/A	3.48055840(32)	35669.3476437(53)
12	3s ² S _{1/2}	-1/2	2	3p ² P _{1/2}	1/2	3	5.404(63)	-1.98889051(18)	-3.3923	N/A	3.48055840(32)	35669.3374666(53)

Table A4. Atomic Data – FeII Isotopic Atomic Mass. The superscript corresponds to the list of references given in Table A7.

A	Atomic Mass [amu]
54	53.9396105(7) ^[5]
56	55.9349375(7) ^[5]
57	56.9353940(7) ^[5]
58	57.9332756(8) ^[5]

Table A5. Atomic Data – FeII Isotopic Mass Shift. The superscript corresponds to the list of references given in Table A7.

Trans	Mass Shift [cm ⁻¹]
1608	-68.45 ^[15]
2433	39.03 ^[15]
2374	48.43 ^[15]
2382	48.13 ^[15]
2600	40.16 ^[15]

Table A6. Atomic Data – Wavelength Table. Note that the FeII 2586 transition from Tables A1 and A2 is not used in the estimation of $\Delta\alpha/\alpha$ for this system, and so has been omitted from this table. Column 1 and 2: atomic species and transition labels^[2]. Column 3: mass number. Columns 4 and 5: magnitude of the F quantum number, which is the vector sum of the total angular momentum for the nuclear state and electron state. Column 6: relative (percentage) strength assuming terrestrial isotopic abundance and equal population in the ²⁵MgII hyperfine energy levels. Column 7: centroid wavenumber. Column 8: vacuum wavelength. Column 9: effective oscillator strength (f_{eff} = oscillator strength multiplied by relative strength. Needed by VPFIT to compute composite Voigt profiles). The superscripts, e.g. ^[3], correspond to the list of references given in Table A7.

Species	Trans	A	F^i	F^j	Relative Strength [%]	Wavenumber [cm ⁻¹]	λ_{vac} [Å]	f_{eff}
FeII	1608	—	—	—	—	62171.623(3) ^[3]	1608.45085(7) ^[3]	—
		54 ^[5]	—	—	5.845(23) ^[6]	62171.580(3) ^[14]	1608.45197(7) ^[27]	0.00339(29) ^[18]
		56 ^[5]	—	—	91.754(24) ^[6]	62171.625(3) ^[14]	1608.45080(7) ^[27]	0.053(5) ^[18]
		57 ^[5]	—	—	2.1191(65) ^[6]	62171.647(3) ^[14]	1608.45024(7) ^[27]	0.00123(11) ^[18]
	2344	58 ^[5]	—	—	0.2819(27) ^[6]	62171.667(3) ^[14]	1608.44971(7) ^[27]	0.000164(14) ^[18]
		—	—	—	—	42658.2440(19) ^[3]	2344.21276(11) ^[27]	—
		54 ^[5]	—	—	5.845(23) ^[6]	42658.2686(19) ^[14]	2344.21141(11) ^[27]	0.00666(12) ^[18]
		56 ^[5]	—	—	91.754(24) ^[6]	42658.2428(19) ^[14]	2344.21283(11) ^[27]	0.1046(18) ^[18]
	2374	57 ^[5]	—	—	2.1191(65) ^[6]	42658.2306(19) ^[14]	2344.21350(11) ^[27]	0.00242(4) ^[18]
		58 ^[5]	—	—	0.2819(27) ^[6]	42658.2188(19) ^[14]	2344.21415(11) ^[27]	0.000321(6) ^[18]
		—	—	—	—	42114.8372(19) ^[3]	2374.46009(11) ^[27]	—
		54 ^[5]	—	—	5.845(23) ^[6]	42114.8678(19) ^[14]	2374.45836(11) ^[27]	0.00183(8) ^[18]
	2382	56 ^[5]	—	—	91.754(24) ^[6]	42114.8357(19) ^[14]	2374.46017(11) ^[27]	0.0287(13) ^[18]
		57 ^[5]	—	—	2.1191(65) ^[6]	42114.8205(19) ^[14]	2374.46103(11) ^[27]	0.00066(3) ^[18]
		58 ^[5]	—	—	0.2819(27) ^[6]	42114.8059(19) ^[14]	2374.46185(11) ^[27]	0.000088(4) ^[18]
		—	—	—	—	41968.0679(20) ^[3]	2382.76397(11) ^[27]	—
	2600	54 ^[5]	—	—	5.845(23) ^[6]	41968.0983(20) ^[14]	2382.76224(11) ^[27]	0.01870(25) ^[18]
		56 ^[5]	—	—	91.754(24) ^[6]	41968.0664(20) ^[14]	2382.76405(11) ^[27]	0.294(4) ^[18]
		57 ^[5]	—	—	2.1191(65) ^[6]	41968.0513(20) ^[14]	2382.76491(11) ^[27]	0.00678(9) ^[18]
		58 ^[5]	—	—	0.2819(27) ^[6]	41968.0368(20) ^[14]	2382.76574(11) ^[27]	0.000902(14) ^[18]
	2600	—	—	—	—	38458.9928(17) ^[3]	2600.17210(11) ^[27]	—
		54 ^[5]	—	—	5.845(23) ^[6]	38458.0181(17) ^[14]	2600.17038(11) ^[27]	0.01397(24) ^[18]
		56 ^[5]	—	—	91.754(24) ^[6]	38458.9916(17) ^[14]	2600.17218(11) ^[27]	0.219(4) ^[18]
		57 ^[5]	—	—	2.1191(65) ^[6]	38459.9790(17) ^[14]	2600.17303(11) ^[27]	0.00506(9) ^[18]
	2600	58 ^[5]	—	—	0.2819(27) ^[6]	38459.9668(17) ^[14]	2600.17385(11) ^[27]	0.000674(13) ^[18]
MgII	2796	—	—	—	—	35760.85414(6) ^[16]	2796.353789(5) ^[27]	—
		26 ^[5]	—	—	11.01(4) ^[17]	35760.9403866(53) ^[16]	2796.34704565(42) ^[27]	0.0673(6) ^[18]
		25 ^[5]	3	1	1.2500(12) ^[18]	35760.9189011(53) ^[23]	2796.34872573(42) ^[27]	0.00764(3) ^[18]
		25 ^[5]	3	2	1.2500(12) ^[18]	35760.9174313(53) ^[23]	2796.34884066(42) ^[27]	0.00764(3) ^[18]
		25 ^[5]	3	3	1.2500(12) ^[18]	35760.9155410(53) ^[23]	2796.34898848(42) ^[27]	0.00764(3) ^[18]
		25 ^[5]	3	4	1.2500(12) ^[18]	35760.9137747(53) ^[23]	2796.34912660(42) ^[27]	0.00764(3) ^[18]
		25 ^[5]	2	1	1.2500(12) ^[18]	35760.8592344(53) ^[23]	2796.35339142(42) ^[27]	0.00764(3) ^[18]
		25 ^[5]	2	2	1.2500(12) ^[18]	35760.8577646(53) ^[23]	2796.35350635(42) ^[27]	0.00764(3) ^[18]
		25 ^[5]	2	3	1.2500(12) ^[18]	35760.8558742(53) ^[23]	2796.35365416(42) ^[27]	0.00764(3) ^[18]
		25 ^[5]	2	4	1.2500(12) ^[18]	35760.8541079(53) ^[23]	2796.35379228(42) ^[27]	0.00764(3) ^[18]
		24 ^[5]	—	—	78.99(3) ^[17]	35760.8373967(53) ^[16]	2796.35509903(42) ^[27]	0.483(4) ^[18]
		—	—	—	—	35669.30440(6) ^[16]	2803.530982(5) ^[27]	—
	2803	26 ^[5]	—	—	11.01(4) ^[17]	35669.3905712(53) ^[16]	2803.52420938(42) ^[27]	0.03369(24) ^[18]
		25 ^[5]	3	2	2.50(2) ^[18]	35669.3725048(53) ^[23]	2803.52642924(42) ^[27]	0.00765(13) ^[18]
		25 ^[5]	3	3	2.50(2) ^[18]	35669.3623278(53) ^[23]	2803.52562935(42) ^[27]	0.00765(13) ^[18]
		25 ^[5]	2	2	2.50(2) ^[18]	35669.3128381(53) ^[23]	2803.53111891(42) ^[27]	0.00765(13) ^[18]
		25 ^[5]	2	3	2.50(2) ^[18]	35669.3026610(53) ^[23]	2803.53031902(42) ^[27]	0.00765(13) ^[18]
		24 ^[5]	—	—	78.99(3) ^[17]	35669.2876697(53) ^[16]	2803.53229720(42) ^[27]	0.2417(16) ^[18]

Table A7. Atomic Data – List of References and Derivations.

Label	Reference	Comment
1	This Work	Labeling convention
2	King et al. (2012)	Labeling convention
3	Nave (2012)	FeII Transition Electronic Configurations, FeII Centroid Wavenumber, and FeII 1608 Vacuum Wavelength
4		Derived from Isotope Mass ^[5] and Isotope Abundance ^[6]
5	Audi et al. (2003)	FeII Isotope Mass and FeII Mass Numbers
6	Taylor et al. (1992)	FeII Isotope Abundance
7	Worden et al. (1984)	FeI Ionisation Potential
8	Bergeson et al. (1996)	Fe II 1608 Oscillator Strength
9	Bergeson et al. (1996)	Fe II Oscillator Strengths
10	Li et al. (2000)	Fe II 1608 Transition Lifetime
11	Biemont et al. (1991)	Fe II Transition Lifetimes
12	Dzuba et al. (2002)	Fe II q -coefficients
13	Porsev et al. (2007)	Fe II q -coefficients
14		Derived from Atomic Mass ^[4] , FeII Isotope Mass ^[5] , FeII Centroid Wavenumber ^[3] , and FeII Mass Shift ^[15]
15	Porsev et al. (2009)	FeII Isotope Mass Shift
16	Batteiger et al. (2009)	MgII Transition Electronic Classifications, MgII Centroid Wavenumber, MgII Mass Numbers, ²⁴ MgII Wavenumber, and ²⁵ MgII/ ²⁴ MgII + ²⁶ MgII/ ²⁴ MgII Frequency Shifts
17	Rosman & Taylor (1998)	²⁶ MgII + ²⁴ MgII Isotopic Abundancies
18		Derived from FeII Isotope Abundance ^[6] , FeII Oscillator Strengths ^[9] , ²⁶ MgII + ²⁴ MgII Isotope Abundance ^[17] , MgII Oscillator Strengths ^[20] , and Assumption of Local Thermodynamic Equilibrium.
19	Kaufman & Martin (1991)	MgII Ionisation Potentials
20	Godefroid & Froese Fischer (1999)	MgII Oscillator Strengths (Theory)
21	Ansbacher et al. (1989)	MgII Transition Lifetimes
22	Dzuba & Johnson (2007)	MgII q -coefficients
23		Derived from ²⁴ MgII Wavenumber ^[16] , ²⁵ MgII/ ²⁴ MgII Frequency Shifts ^[16] , ²⁵ MgII Magnetic Dipole Hyperfine Constants ^[25,28] , and ²⁵ MgII Electric Quadrupole Hyperfine Constants ^[28]
24		Derived from ²⁵ MgII Centroid Wavenumber ^[23] , MgII Transition Electronic Configurations ^[16] , and ²⁵ MgII Magnetic Dipole Hyperfine Constants ^[25]
25	Itano & Wineland (1981)	²⁵ MgII Magnetic Dipole Hyperfine Constants
26		Derived from Lifetimes ^[10,11,21]
27		Derived from Wavenumber ^[3,14,16,23,24]
28	Sur et al. (2005)	²⁵ MgII Magnetic Dipole Hyperfine Constants, and ²⁵ MgII Electric Quadrupole Hyperfine Constants

APPENDIX B: SUPPLEMENTARY RESULTS

Table B1. Model Parameters for the minimum- AIC_c model. The thermally broadened model from Generation 79, as shown in Table B3. This model estimates $\Delta\alpha/\alpha = 3.3 \pm 2.9$ with $\chi^2 = 2762.3$, 101 free parameters and $AIC_c = 3134$ and $BIC = 4185$. Column 2: redshift of the velocity component. Column 3 and 4: Fe II column density and Doppler b-parameters. Column 5 and 6: Mg II column density and Doppler b-parameters. We found one unidentified interloping absorption component and the wavelength, column density and b-parameter is given below the main table. b-parameter and column densities are modelled using H I 1215.67 as the species (i.e. $\Gamma = 6.265 \times 10^8 s^{-1}$ and $f = 0.416400$). The interloping absorption component does not contribute to estimation of $\Delta\alpha/\alpha$.

#	z	FeII		MgII	
		N $\log_{10}[\text{cm}^{-2}]$	b [kms $^{-1}$]	N $\log_{10}[\text{cm}^{-2}]$	b [kms $^{-1}$]
1	1.8369044 \pm 0.0000580	10.91 \pm 1.84	1.72 \pm 3.57	12.15 \pm 1.18	2.48 \pm 5.15
2	1.8370372 \pm 0.0000039	9.85 \pm 0.75	0.20 \pm 1.70	10.64 \pm 0.25	0.29 \pm 2.45
3	1.8374427 \pm 0.0000159	10.54 \pm 0.30	5.79 \pm 1.20	11.60 \pm 0.12	8.34 \pm 1.73
4	1.8375204 \pm 0.0000027	10.42 \pm 0.28	2.58 \pm 0.48	11.46 \pm 0.15	3.72 \pm 0.69
5	1.8376617 \pm 0.0000042	10.23 \pm 0.94	2.30 \pm 0.32	11.71 \pm 0.09	3.31 \pm 0.47
6	1.8377127 \pm 0.0000115	11.38 \pm 0.18	9.69 \pm 2.92	11.95 \pm 0.09	13.96 \pm 4.21
7	1.8377247 \pm 0.0000021	10.97 \pm 0.26	2.79 \pm 0.21	12.15 \pm 0.06	4.01 \pm 0.30
8	1.8379646 \pm 0.0000279	10.08 \pm 1.38	7.06 \pm 4.01	11.30 \pm 0.45	10.17 \pm 5.77
9	1.8381890 \pm 0.0000022	10.44 \pm 0.47	1.97 \pm 0.39	11.66 \pm 0.13	2.84 \pm 0.56
10	1.8382263 \pm 0.0000098	11.86 \pm 0.12	10.76 \pm 2.87	12.22 \pm 0.30	15.51 \pm 4.14
11	1.8382286 \pm 0.0000061	10.95 \pm 1.08	6.37 \pm 0.80	12.49 \pm 0.14	9.18 \pm 1.16
12	1.8383266 \pm 0.0000026	11.43 \pm 0.06	1.79 \pm 0.30	11.94 \pm 0.11	2.58 \pm 0.43
13	1.8383724 \pm 0.0000303	9.99 \pm 1.57	2.19 \pm 3.18	11.05 \pm 0.92	3.15 \pm 4.58
14	1.8385374 \pm 0.0000163	12.40 \pm 0.21	4.60 \pm 0.93	13.20 \pm 0.21	6.63 \pm 1.34
15	1.8385412 \pm 0.0000275	12.37 \pm 0.25	8.56 \pm 1.42	12.43 \pm 0.41	12.34 \pm 2.04
16	1.8385637 \pm 0.0000018	12.23 \pm 0.34	2.14 \pm 0.81	11.97 \pm 1.04	3.08 \pm 1.17
17	1.8386464 \pm 0.0000498	12.05 \pm 0.60	4.07 \pm 2.91	12.90 \pm 0.79	5.86 \pm 4.20
18	1.8386842 \pm 0.0000149	11.80 \pm 1.94	2.13 \pm 2.74	11.18 \pm 9.39	3.06 \pm 3.95
19	1.8387369 \pm 0.0000124	12.13 \pm 3.55	2.66 \pm 3.78	12.66 \pm 3.11	3.83 \pm 5.44
20	1.8387383 \pm 0.0000892	11.82 \pm 5.02	4.63 \pm 10.26	11.99 \pm 9.12	6.68 \pm 14.80
21	1.8388127 \pm 0.0000843	12.03 \pm 2.06	3.28 \pm 7.51	12.44 \pm 3.42	4.73 \pm 10.82
22	1.8388635 \pm 0.0001241	11.42 \pm 9.43	2.72 \pm 9.52	12.72 \pm 3.37	3.91 \pm 13.72
23	1.8388837 \pm 0.0000071	10.35 \pm 9.29	0.65 \pm 2.72	14.41 \pm 9.79	0.93 \pm 3.92
24	1.8388991 \pm 0.0000455	13.04 \pm 1.13	4.09 \pm 8.51	11.33 \pm 9.71	5.89 \pm 12.27
25	1.8389290 \pm 0.0000058	11.32 \pm 2.05	0.46 \pm 1.30	14.43 \pm 8.11	0.66 \pm 1.87
26	1.8389573 \pm 0.0000154	11.85 \pm 0.84	1.60 \pm 0.84	12.38 \pm 0.74	2.31 \pm 1.22
27	1.8389619 \pm 0.0001910	11.87 \pm 5.04	3.36 \pm 7.19	12.34 \pm 3.38	4.83 \pm 10.37
28	1.8390541 \pm 0.0000063	11.37 \pm 0.11	2.00 \pm 0.54	11.86 \pm 0.21	2.88 \pm 0.77
29	1.8390994 \pm 0.0000090	11.59 \pm 0.33	1.60 \pm 1.36	11.55 \pm 0.74	2.31 \pm 1.96
30	1.8391411 \pm 0.0000048	12.23 \pm 0.10	2.20 \pm 0.74	12.27 \pm 0.17	3.16 \pm 1.06
31	1.8391659 \pm 0.0000048	11.59 \pm 0.33	0.54 \pm 0.70	11.37 \pm 0.42	0.78 \pm 1.02
32	1.8392328 \pm 0.0000166	12.04 \pm 0.32	5.12 \pm 2.78	12.24 \pm 0.38	7.37 \pm 4.01
33	1.8392446 \pm 0.0000020	12.13 \pm 0.29	2.19 \pm 0.68	12.20 \pm 0.37	3.16 \pm 0.98
34	1.8393218 \pm 0.0000127	11.50 \pm 0.12	2.73 \pm 0.79	12.05 \pm 0.14	3.94 \pm 1.14
35	1.8393281 \pm 0.0002711	11.07 \pm 1.14	16.57 \pm 15.47	11.84 \pm 0.90	23.88 \pm 22.29
36	1.8393643 \pm 0.0000049	11.62 \pm 0.12	2.05 \pm 0.24	11.98 \pm 0.22	2.96 \pm 0.34
37	1.8398527 \pm 0.0000914	11.11 \pm 0.76	1.24 \pm 3.17	11.82 \pm 1.20	1.79 \pm 4.58
Unidentified Interloper					
	λ [Å]	N $\log_{10}[\text{cm}^{-2}]$	b [kms $^{-1}$]		
1	7960.991 \pm 0.011	11.45 \pm 0.06	2.44 \pm 0.70		

Table B2. Details of the spectral wavelength regions for the minimum- $AICc$ model. The model parameters of the minimum- $AICc$ model are shown in Table B1. Column 1: spectrum label (see Table 2). Columns 2 and 3: species and transition labels. Column 4 and 5: observed start and end wavelength of absorption complex. Column 6: correction applied to the continuum in this region (original continuum is multiplied by this offset). Column 7: correction applied to the zero level in this region (offset added to original zero flux level).

Spectrum	Spec.	Tran.	λ_{start} [Å]	λ_{end} [Å]	Continuum Correction	Zero Level Correction
2000a	Fe II	1608	4563.332	4567.731	1.0026 ± 0.0013	
2000a	Fe II	2344	6735.368	6743.444	1.0041 ± 0.0009	
2000a	Fe II	2374	6758.838	6766.909	1.0010 ± 0.0049	
2000a	Fe II	2600	7375.726	7384.171	1.0032 ± 0.0040	
2000a	Mg II	2796	7932.058	7941.719	1.0395 ± 0.0765	0.0028 ± 0.0007
2000a	Mg II	2803	7952.504	7961.837	1.0145 ± 0.0375	0.0004 ± 0.0028
2000b	Fe II	1608	4562.478	4568.180	0.9990 ± 0.0015	
2000b	Fe II	2344	6650.434	6658.533	1.0035 ± 0.0020	
2000b	Fe II	2374	6735.988	6743.839	1.0002 ± 0.0009	
2000b	Fe II	2600	7376.299	7384.288	1.0039 ± 0.0041	
2000b	Mg II	2796	7932.272	7942.033	1.0395 ± 0.0765	0.0035 ± 0.0010
2000b	Mg II	2803	7952.542	7962.670	1.0191 ± 0.0375	-0.0003 ± 0.0031
2006	Fe II	1608	4562.905	4566.501	1.0082 ± 0.0043	
2006	Fe II	2374	6650.434	6658.533	0.9990 ± 0.0027	
2006	Fe II	2382	6736.266	6744.437	1.0055 ± 0.0016	
2006	Fe II	2600	7376.791	7385.271	1.0015 ± 0.0050	
2006	Mg II	2796	7933.485	7940.107	1.0308 ± 0.0761	0.0036 ± 0.0017
2006	Mg II	2803	7952.814	7960.398	1.0165 ± 0.0378	0.0030 ± 0.0043

Table B3. Comparison of the best-fit models from each generation. Column 1 gives the generation number. Columns 2 to 10 show the thermally broadened models, columns 11 to 19 show the turbulently broadened models. For each generation, the $\Delta\alpha/\alpha$ estimate and number of free parameters k are shown for the three best-fit models, according to each of the three statistics, χ^2 , $AICc$ and BIC . Columns 2,5,8,11,14 and 17 show the $\Delta\alpha/\alpha$ estimates. Columns 3,6,9,12,15 and 18 show the number of free parameters contributing to each model. Columns 4,7,10,13,16 and 19 show respectively the χ^2 , $AICc$ and BIC statistics. The models with a minimum in each statistic are highlighted in yellow. The large jump in the number of free parameters between generation 5 and 6 (from $k = 21$ to $k = 52$) is due to the addition of parameters to correct the continuum and zero levels in the models. When these correction parameters are included in generations 1–5 the bad fit to the data (due to the models lacking the complexity required) leads to obviously bad corrections. Hence these correction parameters are not included until after generation 5. The number of data points is 3258.

#	THERMAL									TURBULENT								
	χ^2			$AICc$			BIC			χ^2			$AICc$			BIC		
	$\Delta\alpha/\alpha$	k	χ^2	$\Delta\alpha/\alpha$	k	$AICc$	$\Delta\alpha/\alpha$	k	BIC	$\Delta\alpha/\alpha$	k	χ^2	$\Delta\alpha/\alpha$	k	$AICc$	$\Delta\alpha/\alpha$	k	BIC
	$[1 \times 10^{-6}]$			$[1 \times 10^{-6}]$			$[1 \times 10^{-6}]$			$[1 \times 10^{-6}]$			$[1 \times 10^{-6}]$			$[1 \times 10^{-6}]$		
1	-465.6	47.5	5 712137.8	-465.6	47.5	5 712147.8	-465.6	47.5	5 712178.2	-510.3	60.4	5 723245.3	-510.3	60.4	5 723255.3	-510.3	60.4	5 723285.7
2	-444.4	42.1	9 585493.0	-444.4	42.1	9 585511.0	-444.4	42.1	9 585565.8	-9.7	21.0	9 520557.9	-9.7	21.0	9 520575.9	-9.7	21.0	9 520630.7
3	-8.8	19.4	13 421947.5	-8.8	19.4	13 421973.6	-8.8	19.4	13 422052.6	28.2	10.9	13 354211.6	28.2	10.9	13 354237.7	28.2	10.9	13 354316.8
4	21.6	10.3	17 242770.8	21.6	10.3	17 242805.0	21.6	10.3	17 242908.3	26.2	8.9	17 240147.3	26.2	8.9	17 240181.5	26.2	8.9	17 240284.8
5	27.2	6.2	21 115307.0	27.2	6.2	21 115349.3	27.2	6.2	21 115476.8	27.0	7.3	21 160988.6	27.0	7.3	21 161030.9	27.0	7.3	21 161158.5
6	6.9	3.8	52 42820.4	6.9	3.8	52 42926.1	6.9	3.8	52 43241.0	9.3	3.7	52 41024.2	9.3	3.7	52 41129.9	9.3	3.7	52 41444.8
7	1.1	3.4	56 34460.0	1.1	3.4	56 34574.0	1.1	3.4	56 34913.0	4.7	3.3	56 34737.7	4.7	3.3	56 34851.7	4.7	3.3	56 35190.7
8	1.4	3.1	60 29019.1	1.4	3.1	60 29141.4	1.4	3.1	60 29504.4	4.0	3.0	60 29153.3	4.0	3.0	60 29275.6	4.0	3.0	60 29638.6
9	-0.3	2.8	64 24340.2	-0.3	2.8	64 24470.8	-0.3	2.8	64 24857.8	4.5	2.3	64 19076.5	4.5	2.3	64 19207.1	4.5	2.3	64 19594.2
10	-1.9	2.0	68 13748.8	-1.9	2.0	68 13887.7	-1.9	2.0	68 14298.8	3.6	2.1	68 14472.1	3.6	2.1	68 14611.0	3.6	2.1	68 15022.1
11	-2.3	1.6	72 9349.1	-2.3	1.6	72 9496.4	-2.3	1.6	72 9931.5	3.1	1.8	72 11182.5	3.1	1.8	72 11329.8	3.1	1.8	72 11764.9
12	-5.3	1.6	76 8445.2	-5.3	1.6	76 8600.9	-5.3	1.6	76 9060.0	5.8	1.7	76 9256.3	5.8	1.7	76 9412.0	5.8	1.7	76 9871.0
13	-4.2	1.6	80 7311.5	-4.2	1.6	80 7475.5	-4.2	1.6	80 7958.6	3.4	1.7	80 8860.4	3.4	1.7	80 9024.5	3.4	1.7	80 9507.5
14	-0.8	1.7	84 5974.8	-0.8	1.7	84 6147.3	-0.8	1.7	84 6654.3	1.3	1.9	84 8710.2	1.3	1.9	84 8882.7	1.3	1.9	84 9389.7
15	9.9	2.0	88 5215.0	9.9	2.0	88 5396.0	9.9	2.0	88 5926.8	0.9	2.0	88 8387.0	0.9	2.0	88 8559.5	0.9	2.0	88 9066.5
16	7.0	2.1	92 4834.2	7.0	2.1	92 5023.7	7.0	2.1	92 5578.4	-0.9	2.0	88 7779.9	-0.9	2.0	88 7960.9	-0.9	2.0	88 8491.8
17	3.5	2.2	96 4619.4	3.5	2.2	96 4817.3	3.5	2.2	96 5395.9	-0.1	2.0	92 7382.1	-0.1	2.0	92 7571.5	-0.1	2.0	92 8126.3
18	0.9	2.3	100 4495.8	0.9	2.3	100 4702.2	0.9	2.3	100 5304.7	-0.2	2.0	92 7574.7	-0.2	2.0	92 7764.1	-0.2	2.0	92 8318.8
19	4.5	2.3	104 4224.5	4.5	2.3	104 4439.4	4.5	2.3	104 5065.8	-4.8	1.9	92 6269.3	-4.8	1.9	92 6458.7	-4.8	1.9	92 7013.5
20	-4.3	2.3	104 4347.0	-4.3	2.3	104 4561.9	-4.3	2.3	104 5188.3	-4.5	1.9	96 5877.8	-4.5	1.9	96 6075.7	-4.5	1.9	96 6654.3
21	-5.1	2.6	108 4343.9	-5.1	2.6	108 4567.4	-5.1	2.6	108 5217.5	-5.7	1.9	92 5934.5	-5.7	1.9	92 6123.9	-5.7	1.9	92 6678.7
22	-1.4	2.5	108 4415.2	-1.4	2.5	108 4638.7	-3.0	2.9	104 5286.9	-3.7	1.9	92 6850.9	-3.7	1.9	92 7040.3	-3.5	1.9	88 7584.5
23	-4.7	3.0	112 4310.3	-4.7	3.0	112 4542.4	-4.7	3.0	112 5216.3	-2.9	1.9	96 6755.0	-2.9	1.9	96 6952.9	-2.9	1.9	96 7531.5
24	-8.6	2.9	112 4262.1	-8.6	2.9	112 4494.1	-8.6	2.9	112 5168.1	-4.6	1.9	97 6572.5	-4.6	1.9	97 6772.5	-4.6	1.9	97 7357.1
25	-11.1	2.9	116 4130.9	-11.1	2.9	116 4371.5	-7.0	2.7	112 5046.4	-5.1	1.8	101 5878.9	-5.1	1.8	101 6087.4	-5.1	1.8	101 6695.8
26	-10.9	3.0	116 3907.9	-10.9	3.0	116 4148.5	-10.9	3.0	116 4846.2	-4.5	1.9	105 5739.3	-4.5	1.9	105 5956.4	-4.5	1.9	105 6588.6
27	-8.5	2.9	120 3827.9	-8.5	2.9	120 4077.1	-8.5	2.9	120 4798.5	-4.3	1.9	109 5729.6	-4.4	1.9	109 5947.9	-4.4	1.9	109 6580.2
28	0.5	2.7	120 3794.1	0.5	2.7	120 4043.4	0.5	2.7	120 4764.8	-4.3	1.9	109 5731.3	-4.3	1.9	109 5956.9	-4.3	1.9	109 6613.0
29	-5.2	2.8	124 3620.0	-5.2	2.8	124 3877.9	-5.2	2.8	124 4623.0	-4.2	1.9	105 5733.2	-4.2	1.9	105 5950.3	-4.2	1.9	105 6582.5
30	-5.3	2.7	124 3571.3	-5.3	2.7	124 3829.2	-5.3	2.7	124 4574.4	-4.2	1.9	109 5740.3	-4.2	1.9	109 5965.9	-4.2	1.9	109 6622.0
31	-5.3	2.7	128 3547.2	-5.3	2.7	128 3813.8	-5.3	2.7	128 4582.6	-4.4	1.9	105 6490.1	-4.4	1.9	105 6707.1	-4.4	1.9	105 7339.4
32	-5.8	2.6	132 3144.1	-5.8	2.6	132 3419.4	-5.8	2.6	132 4211.9	-4.5	1.8	109 5702.8	-4.5	1.8	109 5928.5	-4.5	1.8	109 6584.5
33	-5.7	2.5	136 3073.3	-5.7	2.5	136 3357.3	-5.8	2.5	132 4167.8	-3.8	1.8	109 5625.5	-3.8	1.8	109 5851.1	-3.8	1.8	109 6507.2
34	-5.8	2.5	140 3041.4	-5.8	2.5	140 3334.1	-5.8	2.5	140 4173.8	-3.9	1.8	109 5598.8	-3.9	1.8	109 5824.4	-3.9	1.8	109 6480.5
35	-5.7	2.5	144 3031.0	-5.7	2.5	144 3332.4	-5.7	2.5	144 4195.8	-2.8	1.8	105 6152.6	-2.8	1.8	105 6369.6	-2.8	1.8	105 7001.9
36	-5.6	2.5	144 3030.5	-5.6	2.5	144 3331.9	-5.9	2.4	136 4178.7	-4.2	1.9	97 6467.4	-4.2	1.9	97 6667.4	-4.2	1.9	97 7252.0
37	-4.9	2.7	148 2997.8	-4.9	2.7	148 3308.0	-4.9	2.7	148 4167.7	-4.4	1.8	101 5739.2	-4.4	1.8	101 5947.7	-4.4	1.8	101 6556.2
38	-3.4	2.8	152 2983.5	-3.3	2.7	148 3294.7	-4.2	2.8	144 4164.1	-4.0	1.8	105 5335.0	-4.0	1.8	105 5552.1	-4.0	1.8	105 6184.4
39	-3.1	2.8	152 2979.9	-3.1	2.8	152 3298.8	-3.1	2.8	152 4209.4	-2.5	1.8	105 5745.0	-2.5	1.8	105 5962.1	-2.5	1.8	105 6594.4
40	-2.9	2.8	152 2978.4	-2.9	2.8	152 3297.4	-2.9	2.8	152 4207.9	-2.5	1.8	105 6262.9	-2.5	1.8	105 6479.9	-2.5	1.8	105 7112.2
41	-2.9	2.8	152 2976.4	-2.9	2.8	152 3295.4	-1.5	2.8	144 4204.8	-5.4	1.8	109 5999.2	-5.4	1.8	109 6224.9	-4.2	1.8	105 6860.5
42	-2.6	2.8	156 2973.0	-2.8	2.8	152 3294.8	-2.8	2.8	152 4205.4	-0.5	1.5	109 5196.4	-0.5	1.5	109 5422.0	-0.5	1.5	109 6078.1
43	-2.6	2.8	156 2971.6	-2.0	2.8	152 3290.9	-0.5	2.9	144 4166.0	2.6	1.5	109 4220.9	2.6	1.5	109 4446.5	2.6	1.5	109 5102.5
44	-2.4	2.8	156 2970.9	-2.4	2.8	156 3298.7	-2.4	2.8	144 4167.7	8.0	1.6	113 3554.7	8.0	1.6	113 3788.9	8.0	1.6	113 4468.8
45	-2.3	2.8	144 2912.0	-2.3	2.8	144 3213.5	-2.3	2.8	144 4076.8	8.5	1.6	117 3468.9	8.5	1.6	117 3711.7	8.5	1.6	117 4415.3
46	-1.4	2.8	148 2895.2	0.2	2.7	144 3202.3	0.2	2.7	144 4065.7	12.1	1.9	121 3393.8	12.1	1.9	121 3645.2	12.1	1.9	121 4372.5
47	0.8	2.8	148 2864.8	0.8	2.8	148 3175.0	0.8	2.8	148 4061.9	13.7	1.9	125 3341.5	13.7	1.9	125 3601.6	13.7	1.9	121 4329.2
48	0.8	2.8	148 2863.7	0.8	2.8	148 3173.9	0.8	2.8	148 4060.9	13.4	1.9	129 3310.7	13.4	1.9	129 3579.4	13.7	1.9	125 4348.9
49	1.3	2.8	136 3115.4	1.3	2.8	136 3399.3	1.3	2.8	136 4215.4	13.6	1.9	129 3310.1	13.6	1.9	129 3578.8	9.3	1.5	121 4352.7
50	-0.8	2.9	140 3040.8	-0.8	2.9	140 3333.5	-0.8	2.9	140 4173.3	13.9	2.2	133 3285.6	13.9	2.2	133 3563.0	13.8	1.9	129 4347.0
51	2.4	2.7	140 2939.7	2.4	2.7	140 3232.4	2.4	2.7	140 4072.2	14.0	2.2	137 3262.0	14.0	2.2	137 3548.1	13.8	2.0	133 4347.3
52	2.0	2.7	144 2915.8	2.0	2.7	144 3217.2	2.1	2.7	140 4066.0	14.1	2.2	137 3239.5	14.1	2.2	137 3525.6	9.2	1.8	129 4346.0
53	1.7	2.7	148 2872.4	1.7	2.7	148 3182.5	1.7	2.7	148 4069.5	6.8	1.7	133 3264.1	6.8	1.7	133 3541.5	6.8	1.7	